TWO EXPERIMENTS FOR MEASURING SPECIFIC VISCOELASTIC COHESIVE ZONE PARAMETERS

A Thesis

by

JUSTIN JOEL WILLIAMS

Submitted to the Office of Graduate Studies of
Texas A&M University
in partial fulfillment of the requirements of the degree of

MASTER OF SCIENCE

May 2002

Major Subject: Aerospace Engineering

ABSTRACT

Two Experiments for Measuring Specific Viscoelastic Cohesive Zone Parameters.

(May 2002)

Justin Joel Williams, B.S., Embry-Riddle Aeronautical University

Chair of Advisory Committee: Dr. David H. Allen

A micromechanical model for a viscoelastic cohesive zone has been previously formulated and based on a continuum mechanics model of the damage zone ahead of the crack tip in a polymer solid. The scale of the cohesive zone model is quite small, thus rendering it difficult to obtain the cohesive zone parameters experimentally. Presented herein is an experimental procedure for measuring the crack tip opening, damage zone profile ahead of the crack tip, crack tip opening rate, critical fibril breaking length and fibril diameter, all as a function of location and time. It is then shown that these parameters can be used to completely characterize a viscoelastic cohesive zone model.

DEDICATION

For my brother, Jason, you saved my life.

ACKNOWLEDGEMENTS

I would like to gratefully acknowledge the state of Texas via the Higher Education Coordinating Board for the advanced research program grant number 000512-0262-1999, as well as the Texas A&M University Department of Aerospace Engineering for the opportunity to make this research possible: Dr. Allen and his research group, Chad Searcy, Gary-Don Seidel, Kayleen Helms, and Kyle Clayton, for helping me understand and accomplish the research; and Rick Allen and Andrew Fawcett for all the machine shop work. I would also like to thank Lawrence Livermore National Labs for the use of certain scientific equipment; Luke Penrod for the LabVIEW programming; Carl Storrie and Matt Howell for the AutoCAD work; Rick Littleton and Dr. Helga Sittertz-Bhatkar from the Texas A&M Electron Microscopy Center; Dr. H.J. Sue, Dr. Jim Lu, and Dr. Bradley from Texas A&M Dept. of Mechanical Engineering; Kim Youn-Rak and the Texas Transportation Institute for the asphalt samples and material properties; Dr. Kramer from U.C. Santa Barbara; Dr. Ken White from the University of Houston; Dr. P.G. Beahan and Dr. D. Hull from the University of Liverpool; as well as Dr. K. Pandya and Dr. Williams from British Petroleum. All of your help was invaluable in the development of the research.

TABLE OF CONTENTS

LIST OF FIGURES

FIGURE Page

FIGURE Page

FIGURE Page

LIST OF TABLES

CHAPTER I

INTRODUCTION

Structural failure is an immense problem that has plagued scientists and engineers since the dawn of construction. Structural failure can usually be traced back to the onset of unforeseen unstable crack growth. Within the last century a considerable effort has been put forth to understand and thus predict crack growth before it leads to catastrophic failure. Dramatic disasters like the O-ring failure of the shuttle Challenger, the Aloha Air "pop-top" airline accident, or the collapse of the Petrobras oil rig, the worlds largest, draw world wide attention to the problem, but viscoelastic failure is also a trillion dollar worldwide problem seen on every asphalt roadway across the planet. Solving problems such as these will save lives and prevent the loss of an incalculable amount of money.

The problem sounds quite simple; how can crack growth be predicted and therefore be prevented? Many methods have attempted to solve this problem, but unfortunately this problem is still not completely understood. As will be discussed in section 1.2, many experimental procedures have been developed to investigate and measure certain crack tip parameters, but the problem with these procedures is their inability to measure parameters during crack propagation. Past techniques produce data after the material has already failed.

This thesis follows the style of the *Journal of Engineering Materials and Technology*.

This thesis picks up where other techniques fail. The following pages present techniques for measuring specific crack tip parameters in viscoelastic media during actual crack growth. The experiments herein produce real time images of cohesive zone evolution and crack propagation.

Petroleum based asphalt binders tend to be very similar to rubber cement with respect to their cohesive zones and fibril sizes. Asphaltic binder is the matrix that holds much of the roadways on the planet together. Roadway failure is an immense problem costing billions of dollars a year to fix or repair. Cohesive zone research in asphalt can help to solve many roadway failure problems and potentially save billions of dollars if applied worldwide.

Another material that is particularly applicable to this experiment is chlorotrifluoroethylene/ vinylide fluoride copolymer binder KEL-F 800 or KELF. KELF is the matrix in a nuclear missile detonator. Nuclear missiles have been sitting in launch silos for thirty to fifty years or more. Obviously, if the detonators do not function properly the missiles are not effective in reaching their design goals. Unlike rubber cement or asphalt, the KELF cohesive zone is much smaller. Like many polymers (polystyrene, polyethylene, polypropylene) the cohesive zone and fibrils are not visible to the naked eye or even under large optical magnification. These kinds of materials may appear to undergo brittle fracture due to the smooth fracture surface discernable to the naked eye. This is deceiving because at and around the crack tip the failure is actually ductile. Section 3.1 and 3.1 discusses how this can indeed be ductile fracture at the crack tip even though it does not appear this way at first inspection.

The first experiment to be developed records the experiments while the test is performed under optical microscope equipment. To record crack tip and cohesive zone images while the sample is under magnification in real time requires a steady crack tip. A tensile stage was built that will apply a force equally to both ends of a sample. This was done in order to maintain a steady position of the crack. Also, a system was developed for taking images from the eyepieces of the stereomicroscope and recording them on videotape. Once the video of the crack tip was made, a process was devised for transferring it into a digital format for editing on the computer. The digital environment proved to be ideal for measuring cohesive zone parameters.

The optical developments were an excellent stepping stone into electron microscopy (EM) experiments. Virtually all of the challenges that were overcome in the development of the optical experiments exist in the EM experiments, only on a much smaller scale. Some materials have cohesive zones small enough to require the use of electron microscopy. Unfortunately, samples are preparation intensive for SEM tests. For this thesis it was decided to use the Environmental Scanning Electron Microscope (ESEM) not only because it was available and fairly inexpensive to use, but more importantly because the ESEM does not require any special preparation of the sample.

To do the experiments inside the ESEM, a special tensile stage was built. In the ESEM experiments it is still necessary to maintain a steady crack tip while the sample is tensile tested. For these tests it was necessary to design the stage with much higher

tolerances, due to the high magnification of the ESEM. Even the slightest movement of the crack tip would be visible.

One major difference in the ESEM stage development was the necessity for the entire test to be performed inside the vacuum chamber of the microscope. This put a major restriction on the stage drive system, as there will be no air to cool the motors. KELF was tested and video taped with this stage. Once the video was recorded the transferring, editing, and analyzing process is the same as in the optical experiments. This experiment is detailed in chapter III.

Many different kinds of mathematical models have been developed to better predict when and how fast a crack will grow in solid materials. Cohesive zone modeling is one method that is mathematically representative of a volume ahead of the crack tip where the material is plastically deforming and in many cases fibrillating. The length scale of this fibrillation tends to be material and test rate specific. For example, rubber cement develops very large fibrils and cohesive zones. These details can be seen with the naked eye or under a microscope with small magnification. In figure 1 there are several photos taken from micro scale tensile tests performed on rubber cement under a stereomicroscope. The test was recorded on video. From this video single frames were selected and used to analyze cohesive zone parameters. Details from this experiment are presented in chapter II of this thesis. From the progression of the snapshots it is possible to see the development of the cohesive zone and fibrils within. Each photo has a line drawn over the top of a single fibril or fibrils. The photo is taken just prior to that particular fibrils' failure. In essence, the photo images come from the

video, and the measurements come from the images. The measurements are used to characterize the cohesive zone for crack propagation prediction.

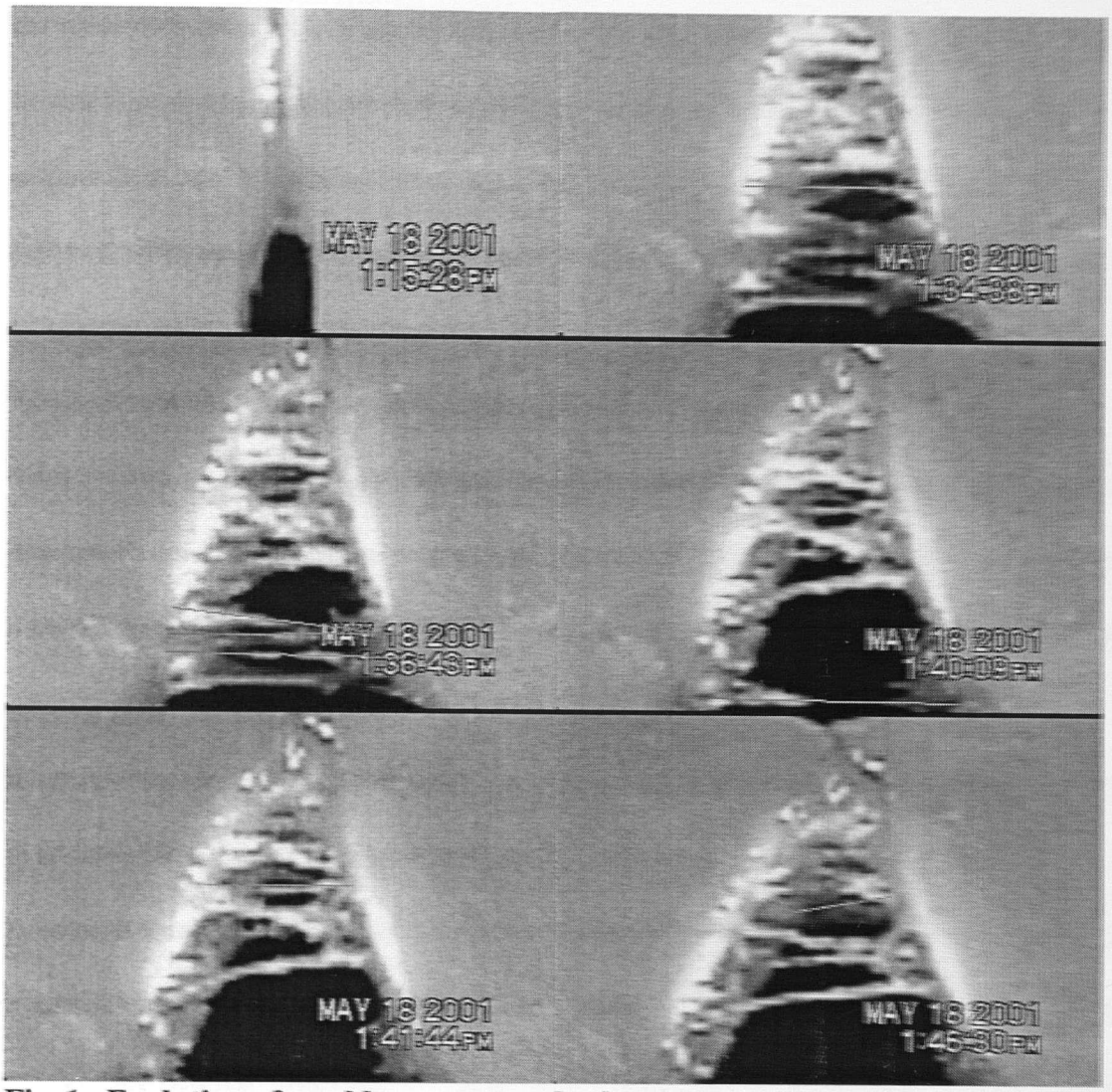

Fig. 1 Evolution of a rubber cement cohesive zone.

1.1 LITERATURE REVIEW

In the past several researchers have developed experimental procedures for determining physical parameters near crack tips. Wang and Kramer (1982a, b), Yang et

al. (1986), as well as Washiyama, Creton, and Kramer (1992) worked with thin films of polymers bonded to annealed copper grids. These grids were used to support the polymers while the whole structure is stressed and plastically deformed. The stiffness of the copper grid holds the stressed polymers so that they could then be placed in a scanning electron microscope. While the grid does hold the deformations of the polymers in place so that the developed fibrils and other cohesive zone parameters are viewable, this procedure does not allow for in-situ real-time examination of the development and evolution of the different crack tip parameters.

Corleto, Bradley, and Brinson (1996) developed a unique technique in which polymeric composites are marked by an electron beam to create a grid of trackable dots. The dot mapping technique is described as a grid of dots that are produced by burning a hole in the gold-palladium sputter coating with electron beam concentration. In essence, the sputter coating left a layer of surface contamination that could be utilized without affecting the characteristics of the material, depending on the material and specimen thickness. The size of the hole or dot, as well as the grid spacing, could be controlled in order to work well with desired strain fields. This technique could prove useful for digital tracking of particular areas on a specimen during real-time experimentation.

Pandya and Williams (2000a, b) have developed another experimental technique for studying medium and high-density pipe grade polyethylene crack properties. These experiments used a notched sample with an initially square cross sectional area. The samples were turned on a lathe and a circular cross sectional area is notched out with a

new area to original area ratio of 1:10. The samples were tested on an Instron MTS machine at varying rates, from rather rapid rates of 50 mm. per min to nearly quasi-static rates of 0.005 mm. per min. After the samples passed peak loads, the samples were sliced open so that the cross sections could be examined by an electron microscope. A vice type clamp was developed to reopen the samples during viewing. This reopened the crack tips and extended the fibrils. Once again this method was postmortem viewing, but has proven to be a good method for gaining quality images of cohesive zone parameters.

Sue (1991) developed a method for the study of fracture toughness measurements in polymeric alloys. This method consisted of using a four-point double notched sample where forces were applied a distance of L apart on one side and L/3 apart on the other. On the side of the forces separated by a distance of L, the notches were milled and precracked at a distance of L/9 apart. Testing samples in this manner allows for pure mode I failure. Ultimately one crack failed before the other. This left a very nicely developed cohesive zone in front of a crack tip. These samples could then be thinly sliced and examined both optically and in an electron microscope. They produced excellent views of the damage in front of the crack tip and details like crack tip opening and fracture toughness. Unfortunately, once again the details were all examined postmortem and details about the evolution of the crack tip and cohesive zone were not revealed.

Allen and Searcy (2001a,b) have postulated a micromechanical model for cohesive zones. This is based on a continuum mechanics model of the damaged region

ahead of the crack tip with a zone of non-zero tractions ahead of the crack tip. This model was particularly beneficial due to its ability to incorporate history and rate dependence in the critical energy release rate in viscoelastic media. Because of the extremely small scale of many cohesive zones, it was very difficult to experimentally determine parameters to be used in the model. In the past, the cohesive zone properties have been postulated in order to make some qualitative predictions. Although the resulting predictions have been somewhat successful, it is important to experimentally determine what the actual cohesive zone geometry is.

1.2 THE MICROMECHANICAL MODEL

The micromechanical model developed by Allen and Searcy resulted in a traction-displacement relationship, equation 1 (2001a,b). The traction-displacement relation in this model is nonlinear and history-dependent, given by

$$T_i(t) = \frac{1}{\lambda}\frac{\delta_i}{\delta_i^*}\left[1-\alpha_1(t)\right]\left[\int_0^t E_{cz}(t-\tau)\frac{\partial \lambda}{\partial \tau}d\tau\right] \text{ (no sum on i)} \qquad (1)$$

where E_{cz} is the viscoelastic relaxation modulus of the undamaged material, δ_i are the opening displacements of the cohesive zone also in the local coordinates of the macroscale crack, and δ_i^* are the components of a material constant representing the fracture mode mixity. τ is a ratio of viscoelastic material properties.

Also, λ is the Euclidean norm of the opening displacements. It is defined in equation 2, where δ_n, δ_r, and δ_s are measured directly from experimental data. These represent the crack opening displacements due to pure mode I, mode II, and mode III

failure, respectively. δ_n*, δ_r*, and δ_s* are material-specific length scale parameters that are scaled according to the experimental results.

$$\lambda(t) = \left[\left(\frac{\delta_n}{\delta_n^*} \right)^2 + \left(\frac{\delta_r}{\delta_r^*} \right)^2 + \left(\frac{\delta_s}{\delta_s^*} \right)^2 \right]^{1/2} \tag{2}$$

In this model α_1 is the time-varying area fraction. As the cohesive zone evolves the fibrils grow in length but reduce in cross-sectional area. α_1 is representative of the area of free space in the cohesive zone cross-section that increases in size (between the fibrils) as each fibril stretches and reduces in cross-sectional area. Fibril failure occurs when a fibril's cross-sectional area falls below a critical value, A_{cr}. The voids and holes produced during fibrillation, or α_1, within the craze can reduce the material volume fraction by as much as 50% or more from that of the parent matrix (Hertzberg, 1987).

The damage parameter, α_1, is related to the representative volume element (RVE). In these experiments A is equal to the planform area of the RVE and thus equal to the length of the cohesive zone multiplied by the sample thickness. A^P is the planform area of the p^{th} fibril, and P is the number of fibrils, see figure 2. A, A^P, and P will all be measured directly from the experimental data.

$$\alpha_1(t) \equiv \frac{A - \sum_{P-1}^{P} A^{p(t)}}{A} \tag{3}$$

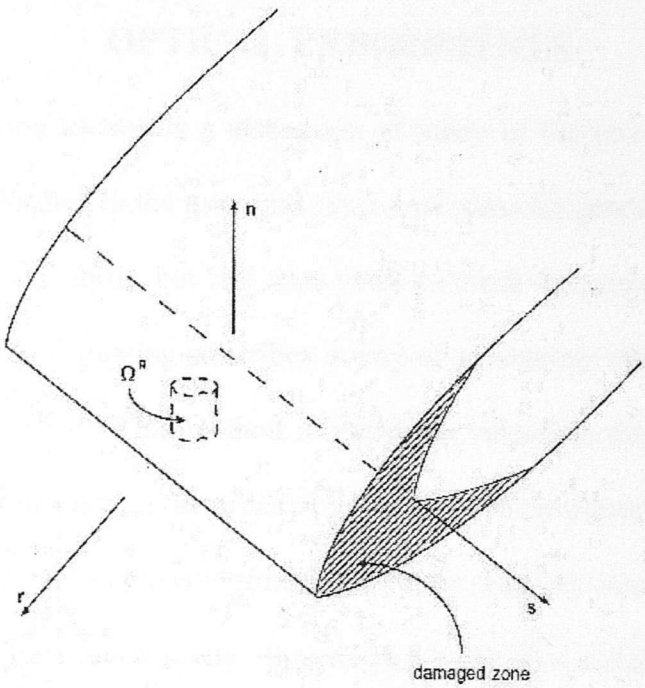

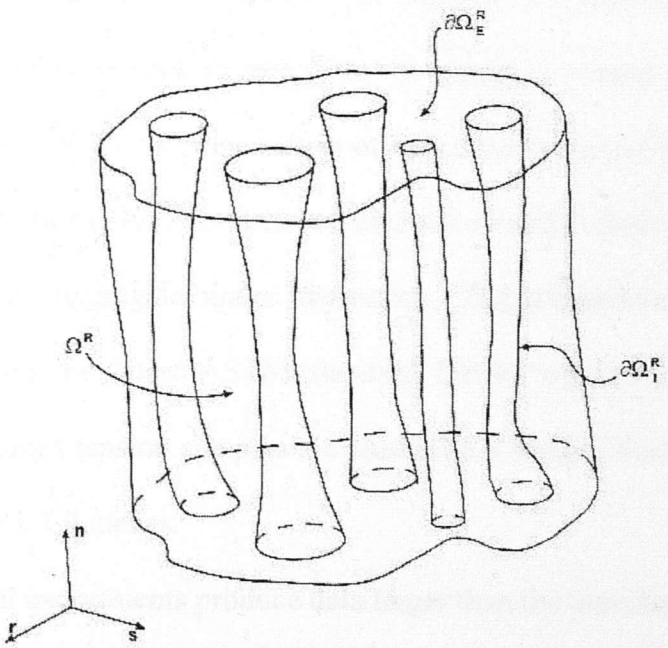

Fig. 2 Damaged region ahead of a crack tip (top). RVE within the damaged region (bottom).

CHAPTER II

OPTICAL EXPERIMENTS

The following section is a discussion of many of the procedures and research that have been performed in the past with some new ideas for producing not just images of cohesive zones and fibrils, but real time video of crack tip propagation and cohesive zone evolution. The following describes a way of producing video images of cracks with optical microscopy. This method is useful for materials that produce crack tips and cohesive zones that are on the order of millimeters or centimeters in length.

In order to create a cohesive zone ahead of the crack tip a compact tension test is performed under a stereomicroscope. For this thesis, binders and glues are tested. It is not practical to make a compact tension sample entirely out of rubber cement or asphalt binder. In the case of asphalt binder, the material is much too viscous at room temperature and tends to stick to everything it comes in contact with. Therefore, a compact tension sample is cut from a sheet of plastic (polystyrene in this case) and then sliced in half. The two halves are then reconnected using the binder or cement. This is representative of the aggregate/binder interaction. The polystyrene samples are all cut in accordance with the latest ASTM standard D5045 originally. Specifically, the standards for compact tension samples are used with a sample thickness of ¼ inch and dimensions of 1.3 x 1.2 inches.

The optical experiments produce data larger than the wavelength of light, but the small scale of all the parameters that are measured in this experiment require the highest amount of precision possible. All measurements are on the micron and sub-micron

level. Because of the small scale, the slightest movement of the crack will cause the points of interest to move out of the field of view. Therefore, a precision tension rack must pull symmetrically from both sides.

In the optical experiments, the compact tension samples are displaced with the Melles Griot Nanomotion II actuators. These motors are capable of displacement steps as small as ten nanometers. This is performed under the objective of the stereomicroscope or in front of the video camera. In cases where the microscope is used, the Panasonic digital cameras receive the image from the eyepieces of the stereomicroscope and relay it through a color sync and stereoscopic multiplexer. This method will produce a stereo image. The stereo image could be used with a virtual reality headset, but wasn't for this research. The benefit of doing this is the production of an image that has virtual depth of field. Potentially, this feature could be used in later developments to help understand the three dimensional evolution of the cohesive zone more completely. For this research only the video from one eyepiece is sent to a video recorder through an S-video output. Crack tip opening and damage zone profile is viewable.

The experiments are recorded on 8mm-video tape through the Sony Hi8 Handicam S-video input or directly through the camera lens. After the test is performed, the video is replayed with the Handicams' VTR mode and then digitized through a Belkin USB Videobus II device. The benefit of digitizing the video is that the computer can add up to another 50x or more of magnification to the images. The software used for these tests typically magnified the image 10-12x and was limited to

32x. Infinite magnification is theoretically possible, but in reality the number of pixels produced by the camera limits usable image magnification. A high-resolution video camera would allow for better digital magnification and image quality. The larger the cameras pick-up devise is the better the analysis will be. From these images, measurements of the crack tip and cohesive zone are made. The video imaging is a key for determining the time dependent measurements.

2.1 OPTICAL EXPERIMENTAL EQUIPMENT

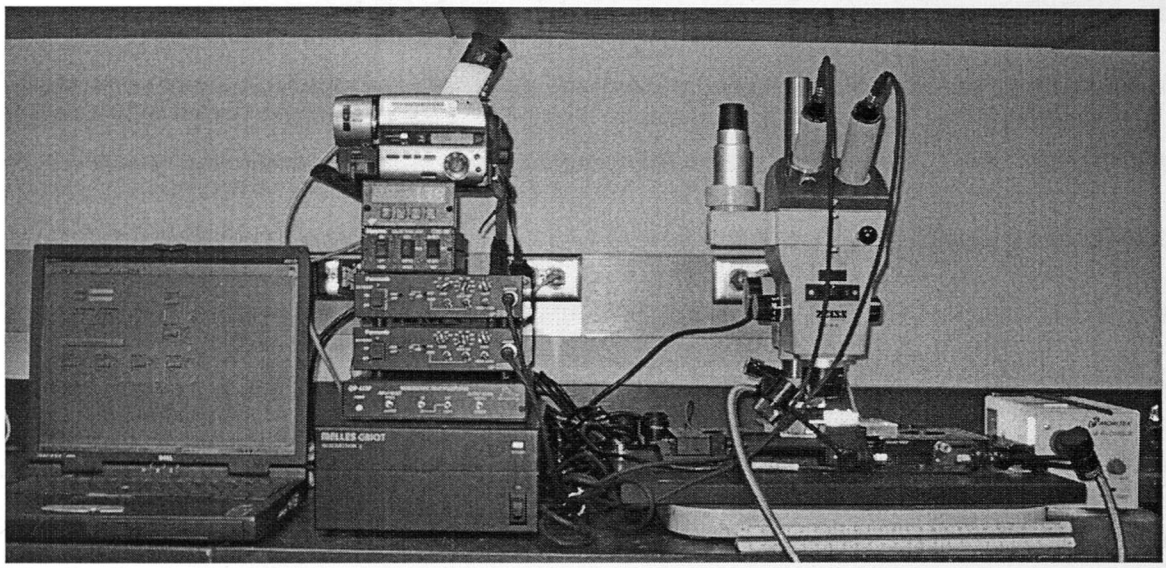

Fig. 3 Optical experimental equipment.

The optical experiments, figure 3, are less expensive than SEM tests due to the added cost of using and/or purchasing SEM equipment. It is important to note that the magnification of the stereomicroscope is not the actual final magnification. The camera's images pass through the multiplexer and then are recorded on the video

camera through its S-video input. This changes the final magnification of the image. The final magnification is dependent on where the images are printed. Obviously, if a parameter that is 1 mm in reality is printed as a one page picture it has undergone more magnification than if it was printed as a half page picture. More importantly than the actual magnification is the image quality and definition. This is how accurate measurements are made.

Of course the initial magnification of the image is reliant on the power and quality of the microscope objective. It is important to remember that as the optical magnification is increased the depth of field is decreased. Optical magnification of 1000x or more is possible, but the depth of field is so narrow that all desired parameters would have to be located in the same plane in order to obtain useful data. This is not useful in reality, cohesive zones are very three-dimensional. A better method for optimizing the analysis is the combination of very high quality low magnification optical objective with an ultra high definition camera that records images with the most pixels possible. These preliminary experiments used a Zeiss stereomicroscope, which has excellent image quality. Unfortunately the Panasonic cameras produced images that are only 320x240 pixels or 76,800 total pixels. It was sufficient for developmental experiments, but a higher definition camera is recommended for a more in-depth analysis. A camera that produces the same image with 1600x1200 pixel dimensions or 1,920,000 pixels total would obviously increase the accuracy of measurements by several orders of magnitude. These tests produced images with between 769 and 1284 pixels per inch.

The strain stage was designed to be symmetric on either side of the test, thus allowing equal and opposite forces to be applied on each of the sample ends. This is necessary to keep the crack tip from moving out of the field of view of the camera. The motors push a translation stage that slides the ends of the samples apart. There is a moment caused by the location of the motors. The motors are not directly connected to the sample ends. They are pushing the edge of the translation stage which intern slides and pulls the end of the sample, see figures 4 and 5. The translation stages are built to a very high tolerance but will rotate within the plane of the test slightly. This rotation causes a minute moment on the sample, but the moment is several orders of magnitude smaller than the forces applied to the sample and is therefore neglected.

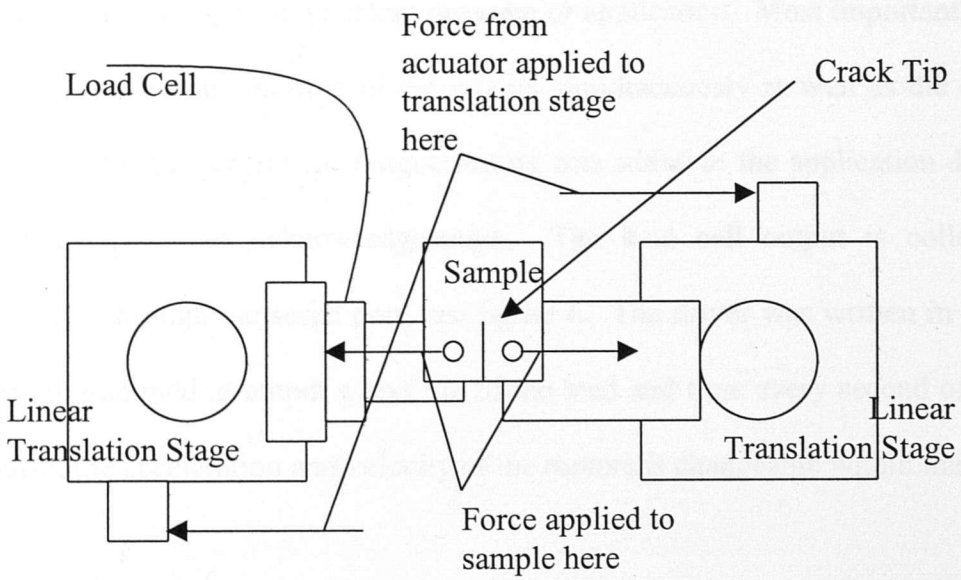

Fig. 4 Schematic of test setup.

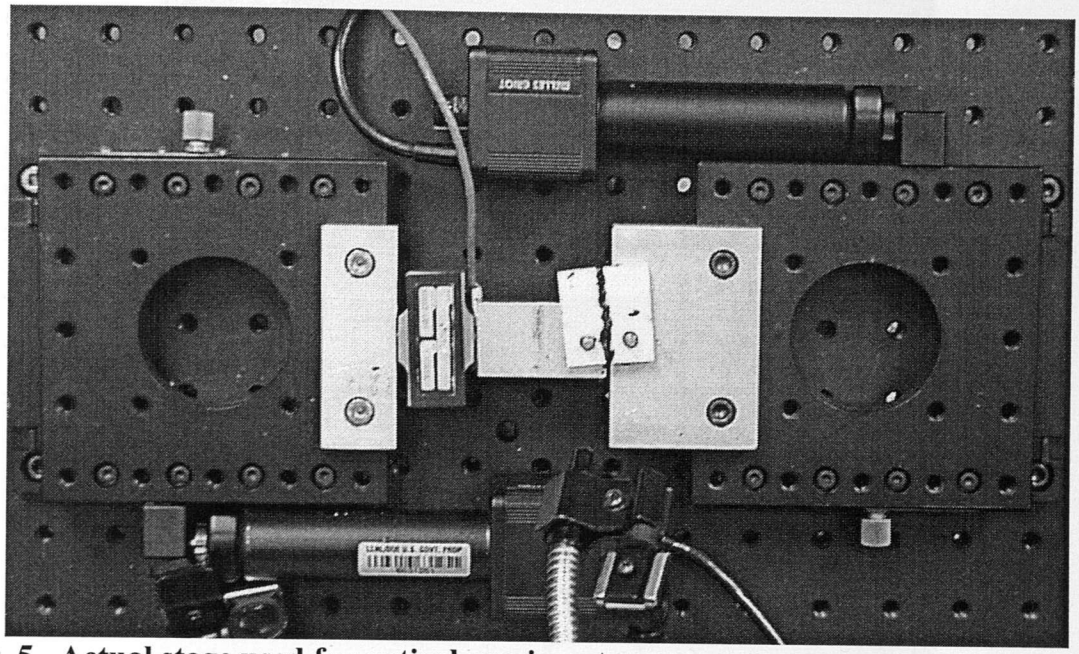

Fig. 5 Actual stage used for optical exeriments.

Melles Griot provided drivers for the Nanomotion II motors. Unfortunately, they did not provide satisfactory control for the experiments. The drivers provided were used as a foundation for a custom program or application. Most importantly, the ability to start and stop the motion of the motors simultaneously as well as the ability to run cycles of the movement for fatigue testing was added to the application drivers by our research team, see acknowledgements. The load cell output is collected by the computer through the serial port, see figure 6. The driver was written in LabVIEW 6i and programmed to output a text file of the load and time every second of the test. Of course, the acceleration and velocity of the motors is changeable within the program.

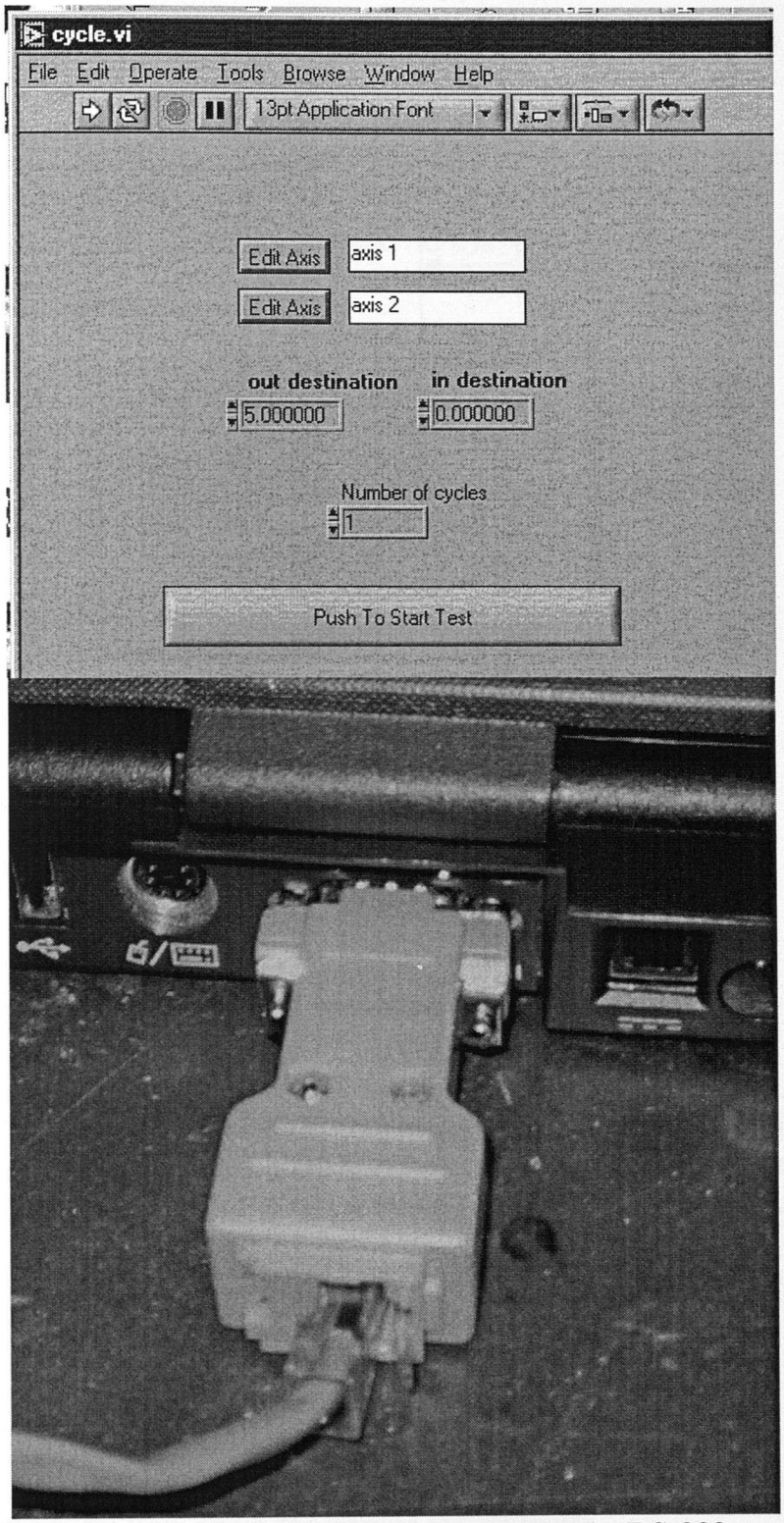

Fig. 6 LabVIEW program for optical experiments (top). RS-232 to serial converter (bottom).

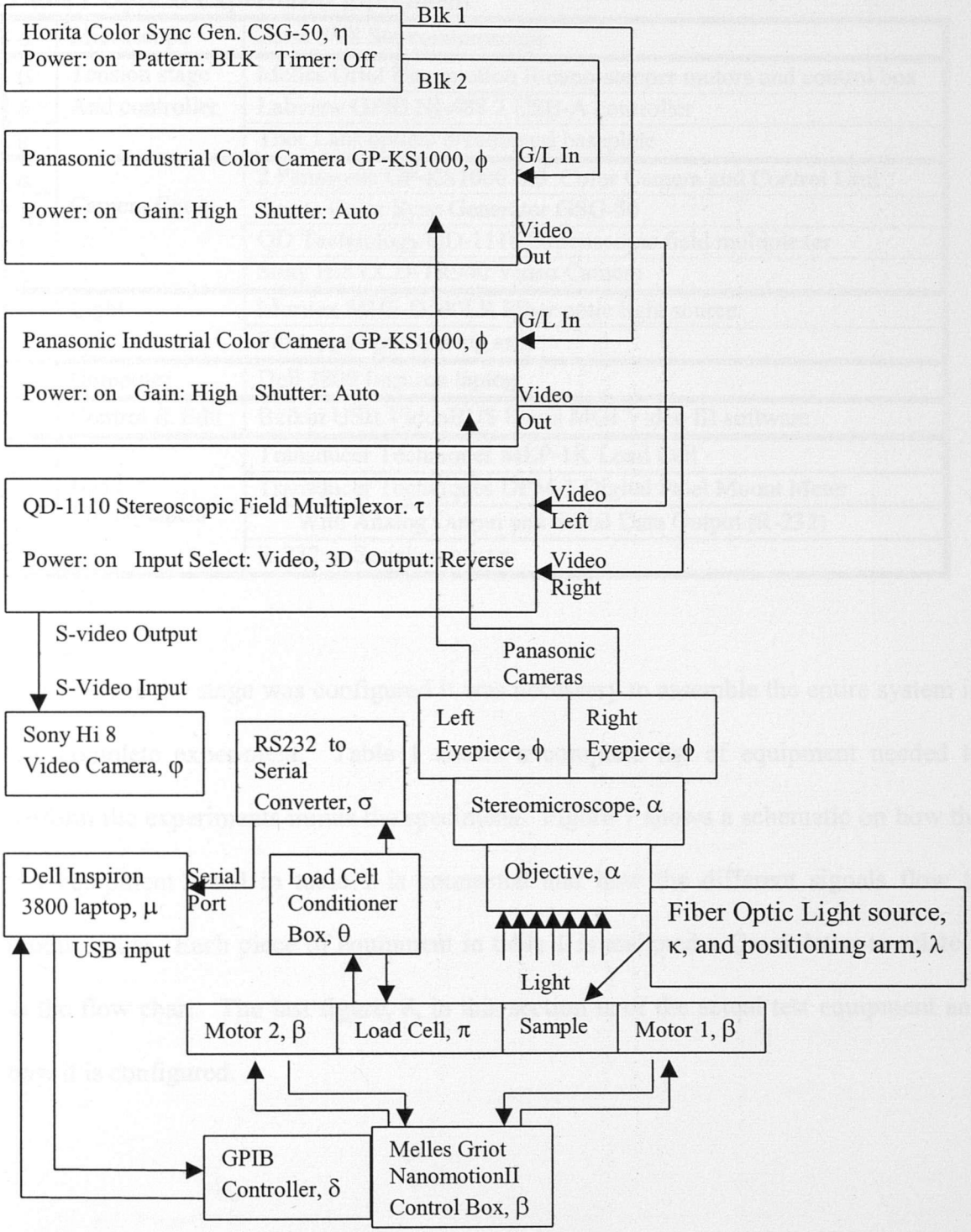

Fig. 7 Experimental flow chart for optical experiments.

Table 1 Optical Experiment Equipment

α	Microscope	Zeiss SV8 Stereomicroscope
β	Tension stage And controller	Melles Griot Nanomotion II nano-stepper motors and control box
δ		Labview GPIB NI-488.2 USB-A controller
ε		Thor Labs optical breadboard baseplate
ϕ	Camera Equip.	2 Panasonic GP-KS1000 Ind. Color Camera and Control Unit
η		Horita Color Sync Generator GSG-50
τ		QD Technology QD-1110 Stereoscopic field multiplexer
φ		Sony Hi8 CCD-TR940 Video Camera
κ	Light	Moritex MHF-D100LR Fiber optic light source
λ		Fiber optic positioning arm
μ	Computer	Dell 3800 Inspiron laptop
ν	Control & Edit	Belkin USB VideoBUS II and MGI Video III software
π	Load Measurement	Transducer Techniques MLP-1K Load Cell
θ		Transducer Techniques DPM-3 Digital Palel Mount Meter
ρ		With Analog Output and Serial Data Output (R-232)
σ		R-232 to Serial converter

Once the stage was configured it was necessary to assemble the entire system in one complete experiment. Table 1 shows a complete list of equipment needed to perform the experiments minus the specimens. Figure 7 shows a schematic on how the test equipment listed in table 1 is connected and how the different signals flow to produce data. Each piece of equipment in table 1 is assigned a Greek letter to relate it to the flow chart. The last figure, 8, in this section is of the actual test equipment and how it is configured.

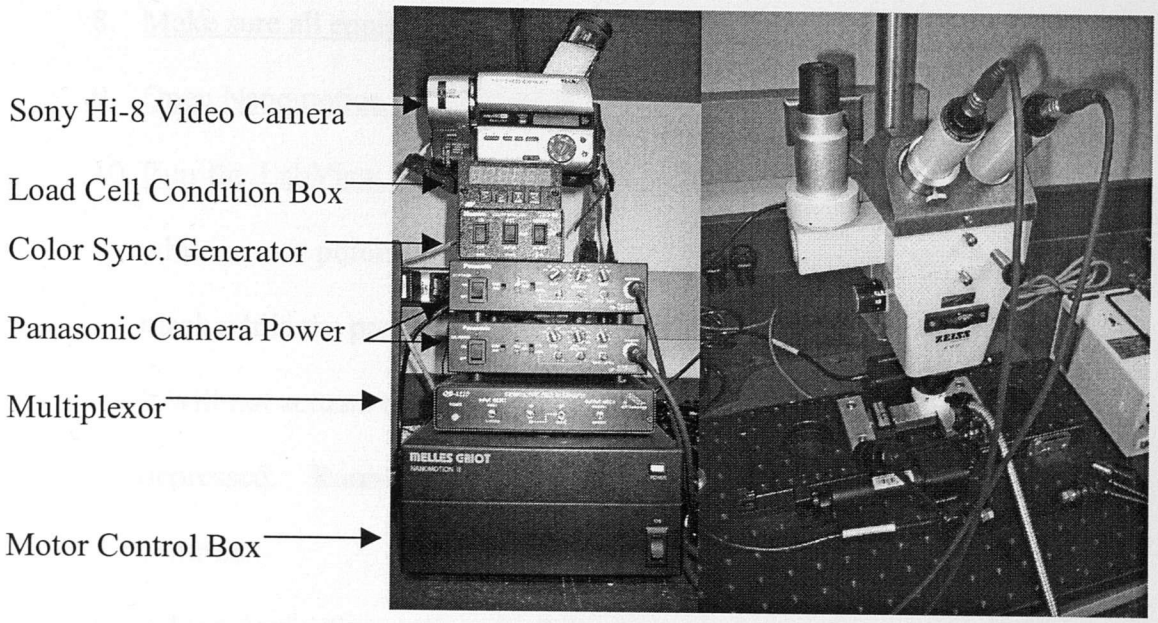

Fig. 8 Control boxes for optical experiments (left). Stereomicroscope (right).

2.2 OPTICAL TESTING PROCEDURE

1. Set up optical equipment according to figure 7.
2. Connect GPIB controller to Melles Griot Controller Box.
3. Bolt Melles Griot translation stage and motors to optical breadboard according to figure 5 configuration.
4. Connect Melles Griot motors to control box ports 1 and 2.
5. Turn on Computer, make sure computer is fully booted up before proceeding to step 6. If GPIB controller is plugged in while the computer is booting up, the computer will not boot properly.
6. Plug GPIB controller into USB port in computer.
7. Turn on Nanomotion II Control Box.

8. Make sure all equipment is turned on and connected correctly.
9. Open Nanomotion II LabView driver.
10. Run the LabView driver. In the upper left hand corner of the window is a white arrow pointing towards the right. When it is depressed it will turn black while the program is running. This is the button that runs the program. It will not actuate the motors UNLESS the "Push to Start Test" button is left depressed. Running the program allows you to edit the axis or motor controls.
11. Adjust destination settings in driver by clicking on the "out destination" and "in destination" boxes. This is the respective position that the motors will cycle between. These values are in millimeters. Choose 15 for out destination, and 0 for in destination. These are good initial values to test the motors.
12. Adjust cycle settings in driver by clicking on the cycle's box. Choose 5 cycles. This is a good number of cycles for testing the motors.
13. Adjust axis settings in driver by clicking on edit axis. This will bring up a new window. In the "Motor Data" box there is another box labeled units. Right click on the units and select Reinitialize to Default Values. When the window is called up again is should read mm. Next, edit the accelerations and velocities of the motors. Accelerations can be up to 1000 mm/s^2 and velocities up to 2.5 mm/s. Both of these are good values to choose while checking out the functionality of the motors. It will move the motors

quickly so that it is not necessary to wait a long time to see if they are responding properly.

14. Push the "Start to Test" button in the driver.
15. Watch the motors cycle through the test. Make sure that they are able to completely move through the positions and have no errors. Count the number of cycles and if the motors are synchronized. If they are not, then there is a problem with the setup. It may be necessary to do this a few times in order to verify that they are working properly. It is a good idea to try different numbers of cycles, accelerations, and velocities to see that the experiment is running properly. Repeat as necessary.
16. Attach fiber optic positioning arm to the breadboard and then the fiber optic end into the clamp.
17. Move the fiber optic into position. It is important to adjust the light so that it is not in between the sample and the objective, but that it is able to shed sufficient light on the sample.
18. Attach sample to stage.
19. Move the microscope into position over the stage. Use the eyepiece to focus image, center crack tip, choose magnification, and adjust the brightness of the light source.
20. Turn on cameras, multiplexor, and color sync. Generator.
21. Turn on video camera. Make sure it is in VTR mode and the S-Video cable is connected.

22. Press record and pause on the camera. An image of the crack tip should appear in the eyepiece.
23. Adjust the microscope focus, the image will be slightly out of focus here as compared to the microscope eyepiece. Most times the focal point for the video cameras is different between the two as well as the image brightness level. It is important that the video recorder image be in focus and well adjusted because that is what is being used for analysis.
24. Enter the positions and number of cycles that is desired for the test.
25. Unpause the video recorder.
26. Run the LabVIEW driver by selecting the run program button and then the "Push to start test" button. It is necessary to first unselect the "Push to start test" button before running the driver. It will still be in the "in" position from the prior test.
27. Repeat as necessary.

2.3 CALIBRATION OF EXPERIMENT

Calibration of the stepper motor displacement is an important factor in the accuracy of the tests. Actual displacement of the motor extension is measured with a caliper micrometer with a resolution of +/- 0.001 meter. This is compared to what the motor was commanded to do. This was done for both motors. The manufacturer has also done calibration and repeatability tests on the motors. Each motor is certified to have an accuracy of +/- 1 micron and a bi-direction repeatability of better than +/- 100

nanometers. Typical bi-direction repeatability is around +/- 20 or 30 nanometers even though the guaranteed performance is +/- 100 nanometers.

The source of this error has been narrowed to three things by Melles Griot, tooth pitch error, torque errors, and lead screw error. Tooth pitch error is the deviation of the tooth to tooth spacing. Torque error is described as the sinusoidal increase or decrease of the microsteps within the tooth pitch. Lastly, the lead screw error is the main contributor to overall accuracy. This is the placement of the zero position while the power is off to the motors. This is only a problem when using the motors to make absolute measurements. Thermal influence was not investigated.

2.4 DATA ACQUISITION AND ANALYSIS

Data Acquisition for these experiments comes in two parts. The Load cell provides highly accurate data about the load being applied to the sample ends. Granted there is some translation or movement of the load cell as it is compressed, but the compression of the load cell is several orders of magnitude smaller than the translation of the stage, and therefore is considered to be negligible. The same load cell will be used for both optical and ESEM experiments. It is important to remember that this is not necessarily going to translate to the force on the fibrils. For this experiment the force applied to the ends of each fibril will be determined analytically through viscoelastity and the displacements of the fibrils.

The load cell used in this experiment is manufactured by Transducer Techniques. The company has a reputation of producing excellent equipment and

published superior accuracy. Their MLP loadcells have a nonrepeatability of 0.05%, Hysteresis of 0.1% and a zero balance of 1%.

The strain in the samples is determined through the video imaging. The video of the samples under tension causes the deformation, and this is recorded on videotape. This tape is then digitized on the computer, and the net change in length of the sample fibrils, crack tip opening, etc. is determined through pixel counting from frame to frame of the video. The video image produced is 3.33 inches by 2.5 inches, or 320 by 240 pixels, as viewed on screen. An object of known length is viewed and recorded. The still image of this object is used to count pixels across the length of the object. Counting the number of pixels in the length of the image and some simple division produces the length of a single pixel. Now, as the videos of the tests are reviewed a single frame is captured precisely before each fibril's failure. This single frame is digitally enlarged using any commercial photo editor. With the known length of each pixel, dimensions of the different parameters in the cohesive zone image can be measured.

CHAPTER III

ESEM EXPERIMENTS

The second experiment was designed to perform the same kind of test as the first, but be conducted inside an Environmental Scanning Electron Microscope (ESEM) and produces images of much smaller cohesive zones and fibrils. Some materials produce cohesive zones so small that they cannot be seen optically because the fibrils are smaller than the wavelength of light. In these preliminary developmental tests the cohesive zone is not smaller than the wavelength of light, but it is smaller than what can be usefully viewed under optical magnification. As mentioned in chapter II, large optical magnification reduces the field of focus to the point where the image is not useful for this experiment. SEM'S in general produce images with significantly greater depth of field at much larger magnifications than can be done optically. This means that the ESEM produces images with increased clarity of significantly smaller details than can be done optically. For these experiments a tensile stage was custom built to perform constant strain rate experiments inside the ESEM.

The ESEM stepper motor drives a shaft that is connected to gears, which are inturn, connected to two counter-threaded screws. This is the actuation that displaces two clamps that are connected to the samples. Ultimately, the same compact tension experiment that was previously performed optically is now being viewed on a much smaller length scale. This experiment was used to test KELF. Because KELF is not as viscous as asphalt, it was not necessary to prepare the sample in the same manner. However, after some modification of the stage, a coupon similar to the shape of a

standard tensile test coupon was used. A razor mark in the center of the coupon acts as a precrack. The magnification used in the ESEM tests (100x-1000x typically) is so large that the standard method of precracking produces much too large of an area to examine. Of course, like other polymers, maximum magnification is limited by beam intensity. Electron beam concentration has been known to melt or deform polymers at high magnification levels if the beam focus is left in one spot for too long of a period of time.

3.1 DUCTILE FRACTURE

In *Fractography* (1999), Hull makes a very good point about the idea of ductile fracture and its connotations. The idea of ductility in fracture projects the image of large deformations and significant amounts of necking before failure. Indeed this is not entirely incorrect, but it is important to not be deceived into thinking that the fracture surface will appear this way to the naked eye. Hull points out that the length scale of some ductile fracture may appear to be smooth to the feel or touch and resemble brittle fracture, but have plastic deformations and nucleation on the microscale. On a much smaller scale (~μm) the surface of some fractured polymers will be highly fibrillated with a large number of holes and voids. The highly fibrillated appearance is a result of the nucleation or formation of holes and voids inside a craze zone. Therefore it is important to remember that first appearances on the macroscale may be entirely different than the microscale. Herein lies one of the major stumbling block in the area of polymer fracture research. See figure 9 for a good example of this.

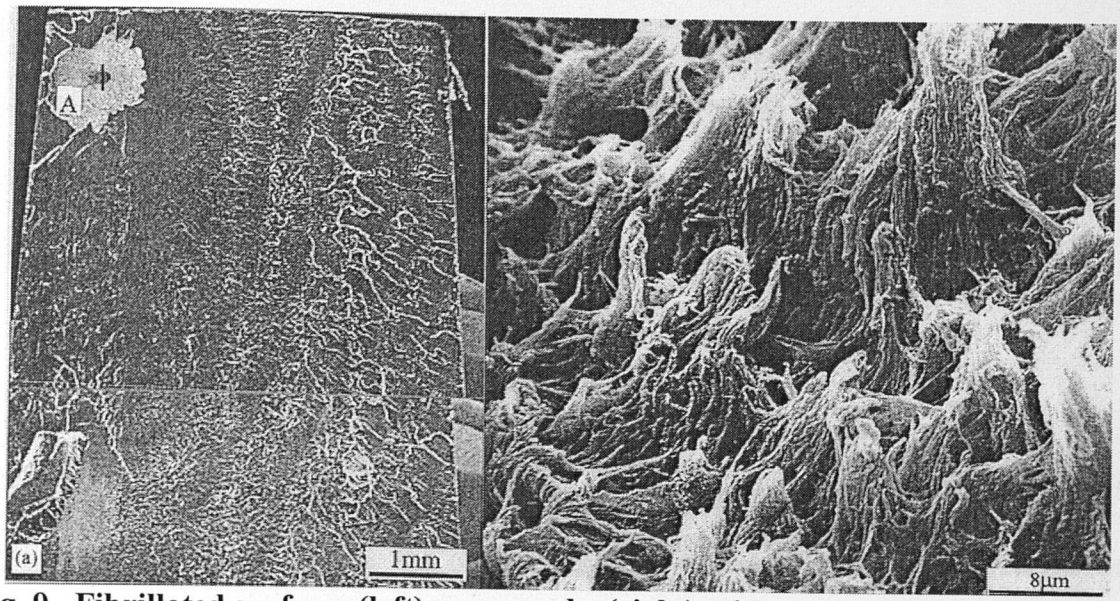

Fig. 9 Fibrillated surfaces (left) macroscale, (right) microscale. Reproduced with permission from Hull.

Hackle surfaces are commonly found in much fractography. Hackle is a very rough surface with irregularly oriented facets. The direction of the facet are aligned parallel to the direction of crack propagation. In a study done by Hibbs and Bradley (1987) several graphite/epoxy systems were studied. Real time observations and postmortem SEM observations were conducted to study the micromechanical processes of delamination failure. The conclusion was drawn that in ductile systems there is generally a lack of any distinct hackle formation like found in more brittle systems (i.e. brittle microcracking). Hackles do not develop because of the resin ductility. Instead the failure is due to yielding and deformation.

3.2 FIBRILS

Many thermoplastic materials, especially those with higher molecular weights, will tend to undergo extensive drawing and plastic deformation. This drawing, or

extensive plastic deformation parallel to the load application also causes molecular orientation parallel to the drawing. As the long chain molecules become more oriented the result is the material being stronger in this direction. This is due to the covalent bonds within the polymer chains which are significantly stronger than that of the Van der Waal's forces between the whole chains (Hull, 1999).

Suresh explains that cyclic deformation or advancing fatigue failure is due to nucleation, growth and breakdown of crazes (Suresh, 1991). At a finer scale it can be seen that inside the craze zone the material is being drawn out more extensively in one direction or fibrillating, see figure 10. It is important to note that the craze zone will develop normal to the uniaxial tensile stress within the material while fibrils develop parallel to it. As the fibrils reach their maximum length or critical breaking length, they each fail individually. This is the propagation of the crack tip.

It is important to also discuss the size and length of the fibrils. Fibrils will vary in length and size depending on the material. Certain thermoplastics, like polystyrene, produce very small fibrils, on the order of 200 to 400 Å. (Beahan, Beavis, and Hull, 1971) Other materials may produce fibrils much larger in scale. For example, rubber cement tends to fibrillate on the order of millimeters or larger.

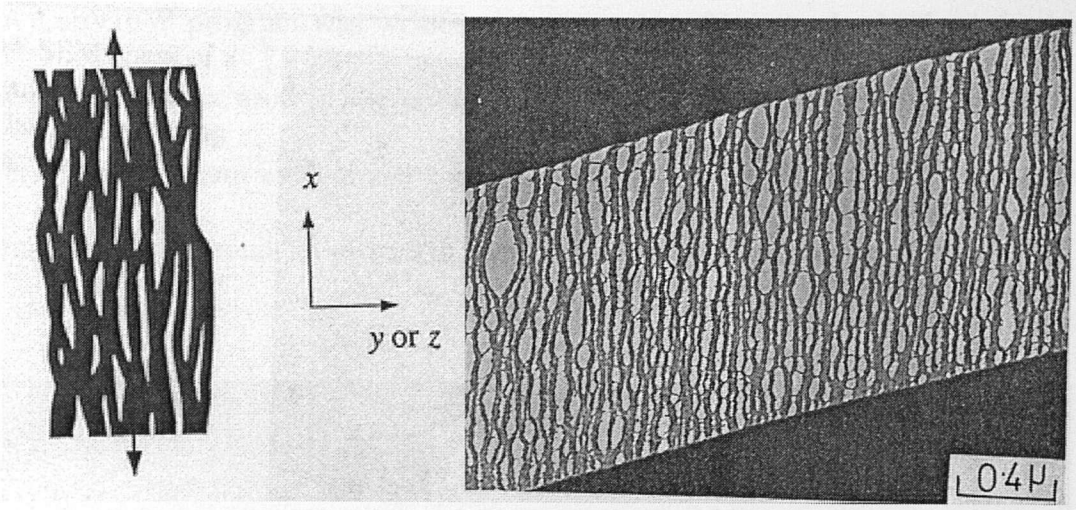

Fig. 10 Fibril schematic (left). TEM micrographs of polystyrene fibrils (right). Reproduced with permission from Hull.

3.3 ESEM EXPERIMENTAL EQUIPMENT DEVELOPMENT

The ESEM experiments required a special tension to be built in order to apply a load to a sample while under the electron beam, and can be seen in figures 11 and 12. This stage was built out of 316 steel. 316 steel has very low magnetic qualities, and thus reduces the amount of interference the metal will have with the electron beam. The Electroscan ESEM has stepper motors with drive shafts built into the door of the microscope. These motors are normally used to rotate or tilt a sample pedestal. This drive shaft is connected to the tensile stage gearbox and drives the opening or closing of the grips. The amount of tensile or compressive force that can be applied to a sample is limited by the amount of torque the motors can produce. At this point the controlling of the motors is limited to an on/off fixed speed. Because of this, the grips are opened at a constant strain rate.

A LabVIEW program was written to acquire data from the loadcell. It is the same subroutine that is used in the optical experiments, but without the Nanomotion controller. This program evaluates the load being applied and writes it to a text file approximately every second. A picture of the program text box can be seen in figure 13.

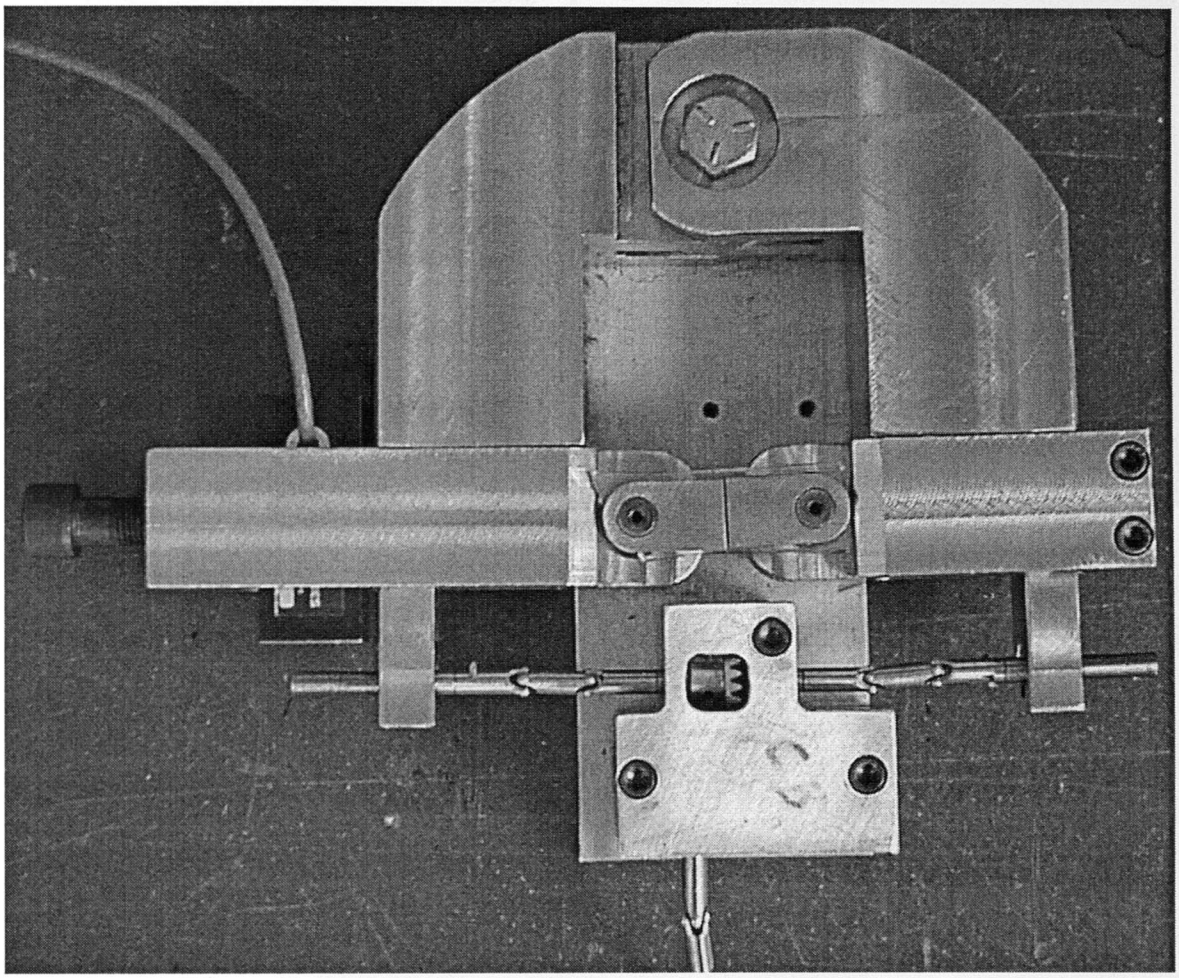

Fig. 11 ESEM tensile stage.

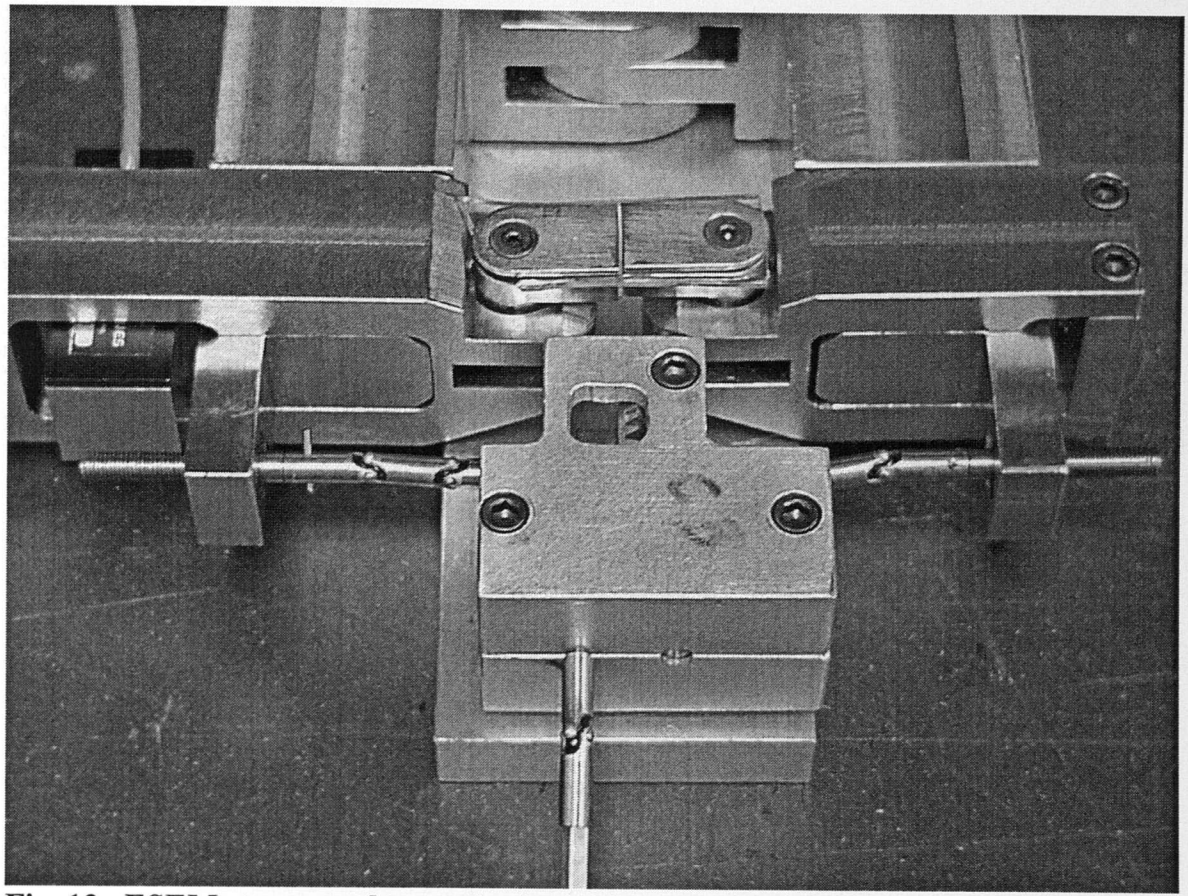

Fig. 12 ESEM stage gearbox and grips.

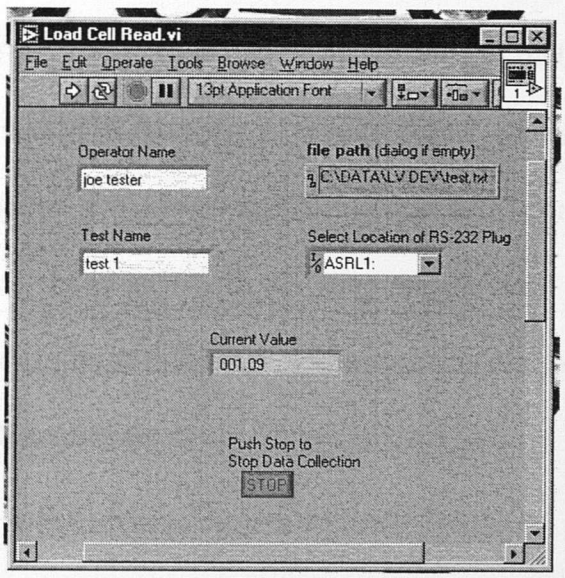

Fig. 13 LabVIEW program for load cell data collection in ESEM experiment.

The ESEM Stage was based on several other already existing SEM stages. The Technische Univsitat Darmshtadt developed an excellent stage for testing ceramics in the SEM. The Darmshtadt stage plans can be seen in figure 14. These plans were examined and modified for our purposes, see figure 15. The ESEM design required more displacement of the grips for polymer testing. The Darmshtadt stage had only a few microns of displacement, much too little for our needs. Originally a piezoelectric actuator was used in our development, like that used in the Darmshtadt stage. The benefit of using a piezoelectric actuator is the nearly instantaneous actuation response. This would allow for excellent control of the experiment. Large displacement piezoelectric actuators, with enough displacement for our needs, occupied much too much space in the design and were too expensive.

Once the piezoelectric actuator was removed from the plans, a new design for actuation or displacement of the grips was needed. The Texas A&M Electroscan ESEM has two stepper motors built into the microscope. These are used to rotate and tilt samples inside the ESEM. For The tensile tests the sample pedestal stage is removed, thus allowing for the use of these motors to actuate the displacement. The motors' driveshaft is connected to a gearbox that simultaneously turns oppositely threaded screws which intern will open and close the stage arms. This proved to be the most economical way to produce large displacements without an overly complex design while utilizing already available equipment.

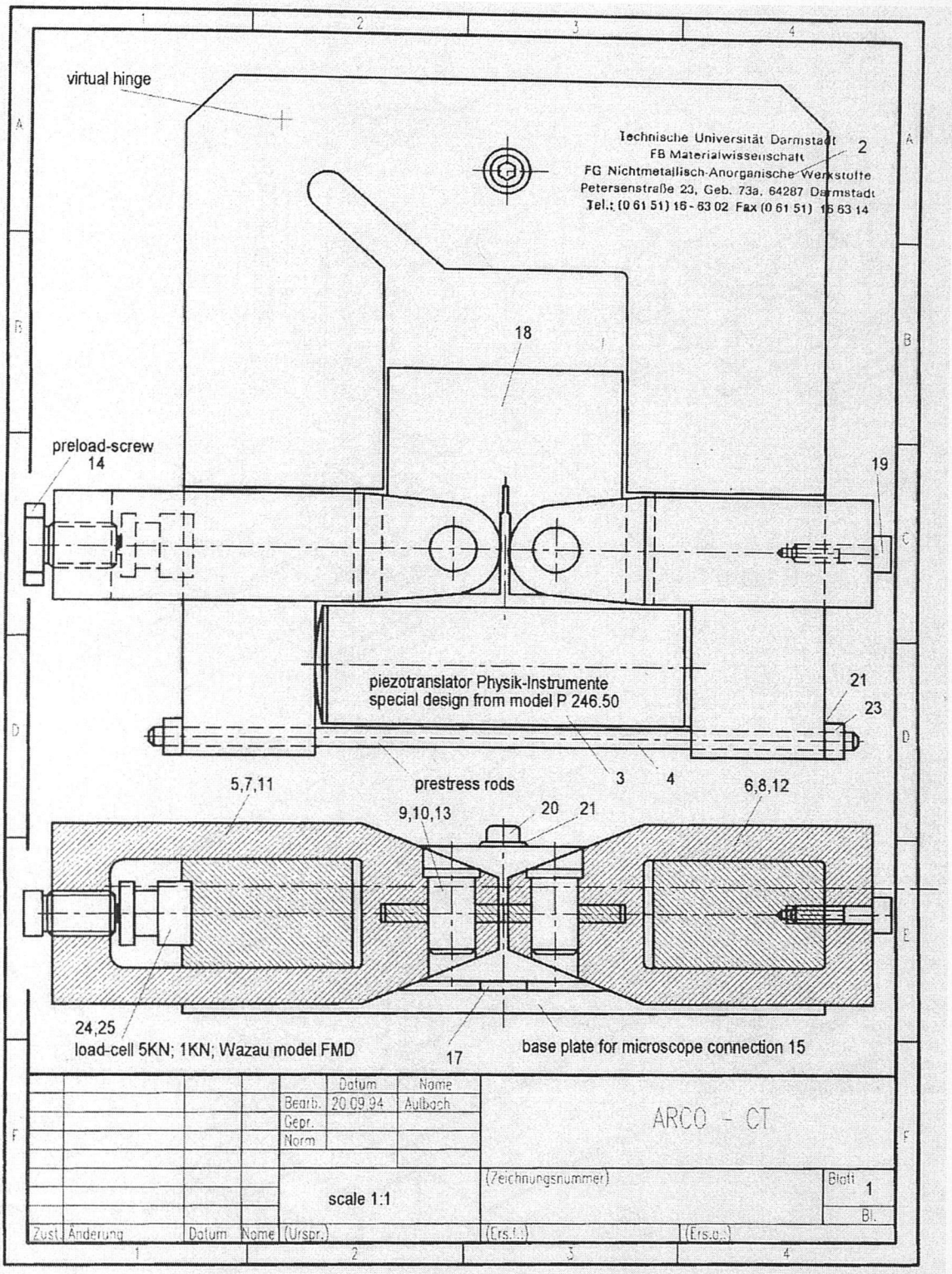

Fig. 14 Plans for the Darmshtadt SEM stage.

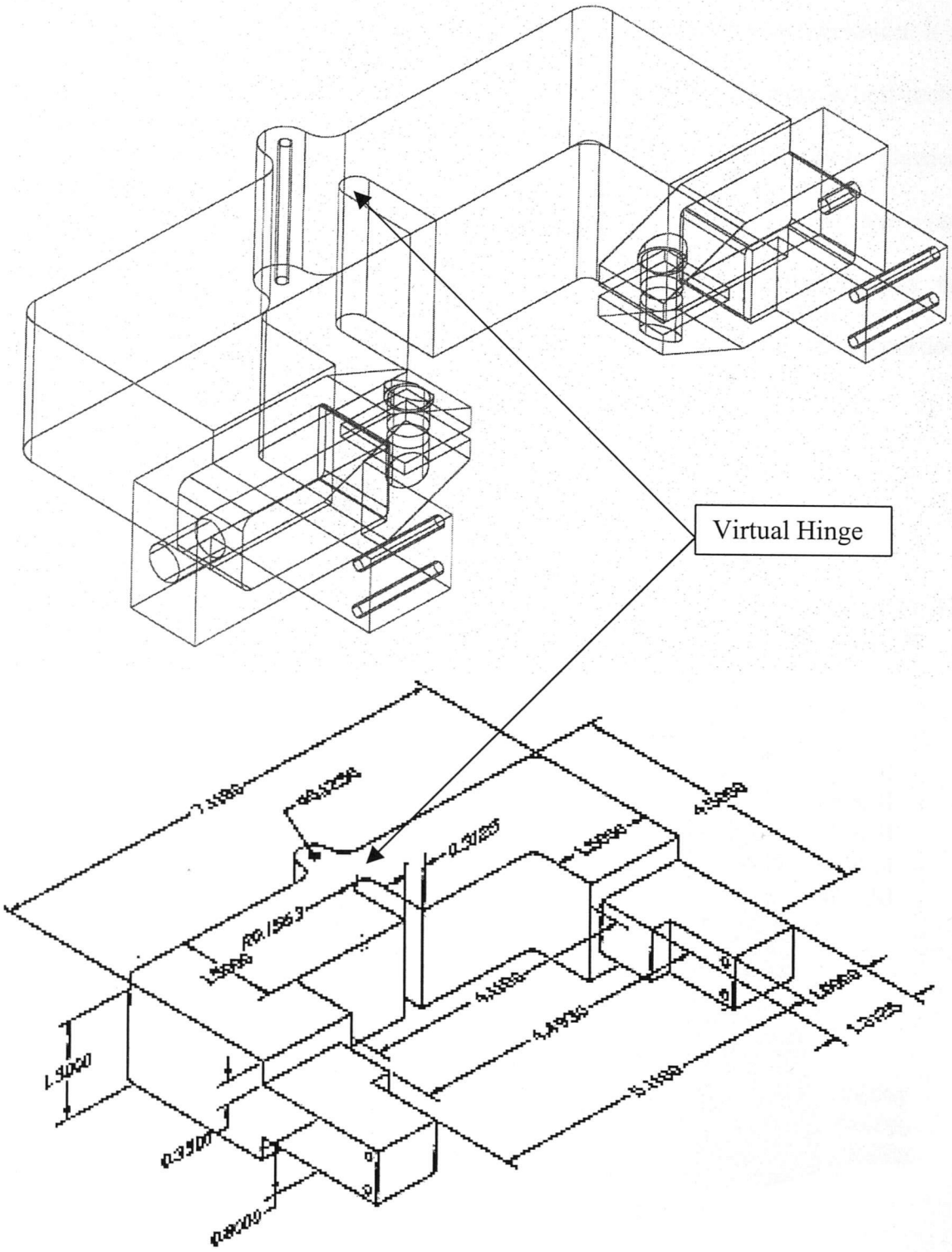

Fig. 15 Piezoelectric stage with modified virtual hinge and large piezo-actuator.

In order to produce symmetric movement of the two arms, the virtual hinge was moved to the center of the design, figure 15 and 16. After further examination, it was not known whether the large displacement of the arms (approximately a half-inch on both sides) would produces a stress concentration that was large enough to plastically deform the virtual hinge. A 3-D finite element mesh was made in FeMAP and a stress analysis was performed in NASTAN. This analysis predicted the stresses were sufficient to produce yielding at large displacements. Thus, this design was modified to use a real hinge instead of a virtual hinge.

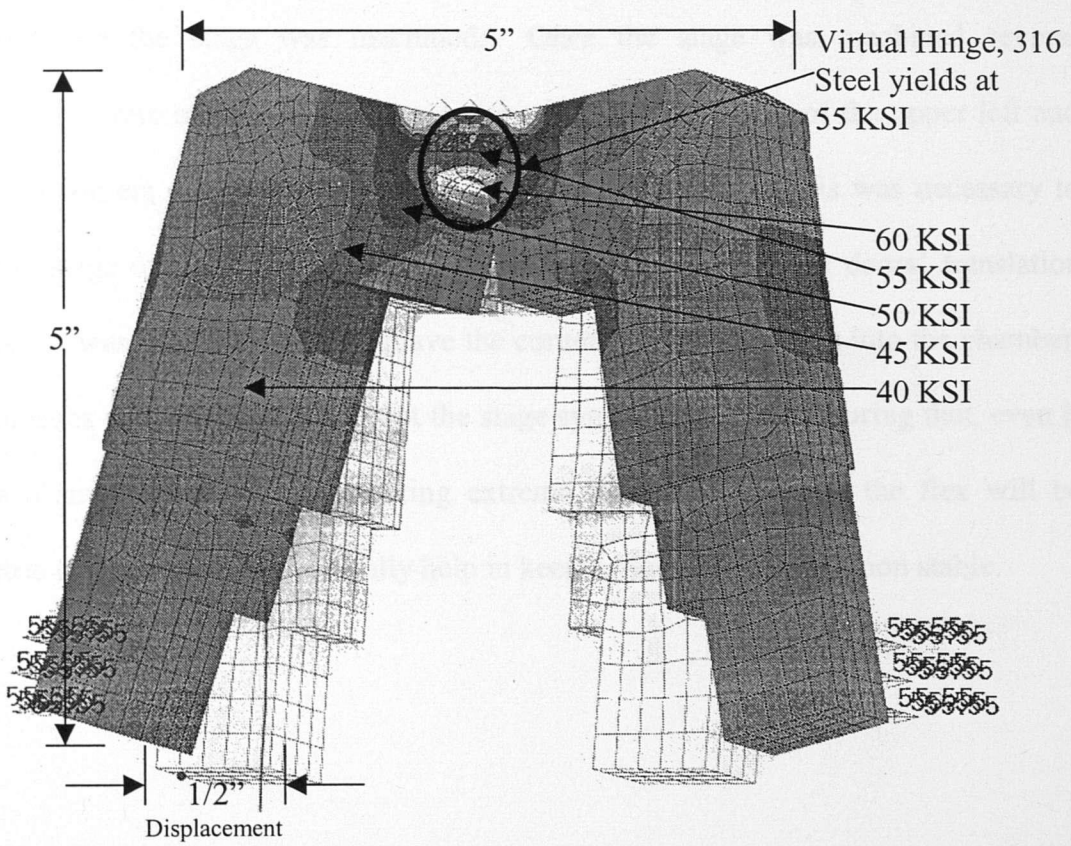

Fig. 16 FEM stress analysis plot of σ_{xx}.

One concern with the hinge design was the possibility of out-of-plane movement when the body arms are moved. The hinge was designed to have several layers overlapping, and was machined to the highest tolerances possible. This made a very tight fit and would minimize any out of plane movement. This hinge design can be seen in the three-view drawing in figure 17. Figure 18 shows the grip design for this stage. It is important to note that the grips are not identical. The left grip is slightly longer to allow for a load cell to be placed into the stage. Figure 19 shows the actual load cell in and out of the grip. This stage was designed to use a Transducer Techniques Mini Low Profile (MLP) load cell.

This design seemed to be the most promising, and at this point the metal was purchased and the stage was machined. Once the stage was machined several modifications were made to the above design. The filleted edges of the upper left and right hand corners of the stage arms had to be trimmed more. This was necessary to allow the stage to enter the ESEM chamber while attached to the doors' translation platform. It was only necessary to shave the corner of one edge to fit into the chamber, but both sides were shaved. This kept the stage symmetric. Thus ensuring that, even if there is a small amount of flex during extreme loading conditions, the flex will be symmetric to both sides and hopefully help in keeping the crack tip position stable.

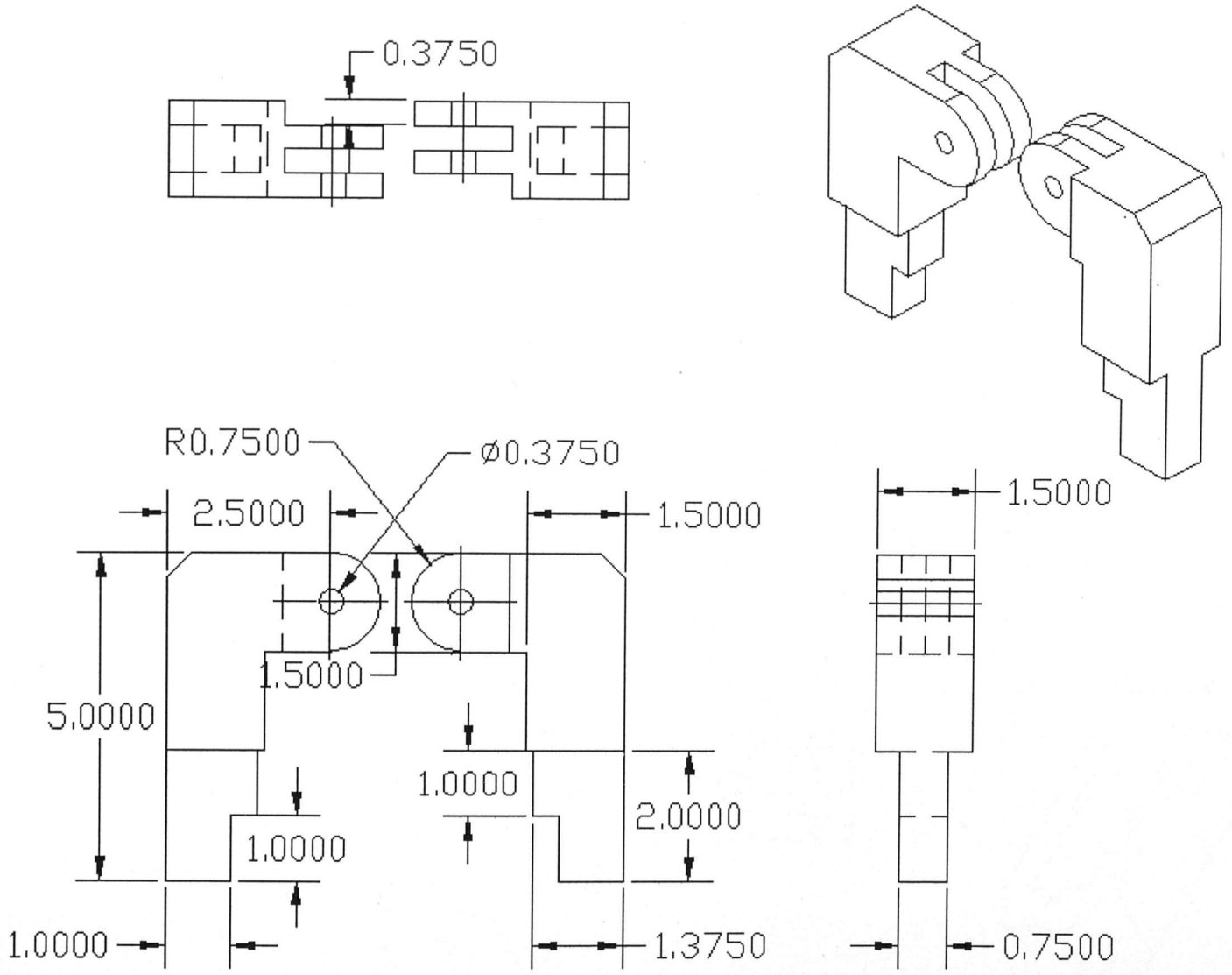

Fig. 17 Three view and isometric drawings of hinge design.

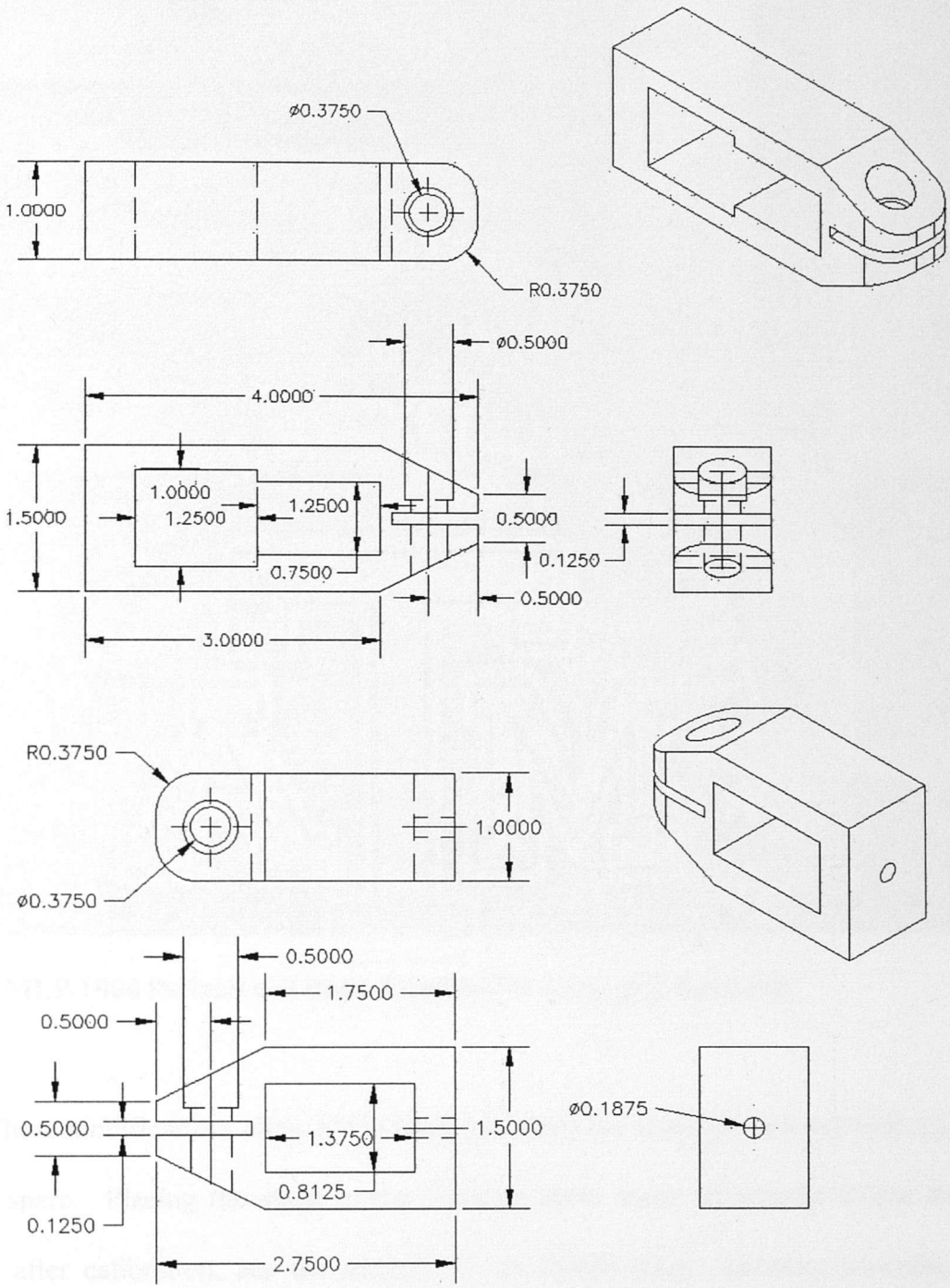

Fig. 18 Three view and isometric drawings of grip design.
Note that the left grip (top) is slightly longer allowing for a load cell to be put into place.

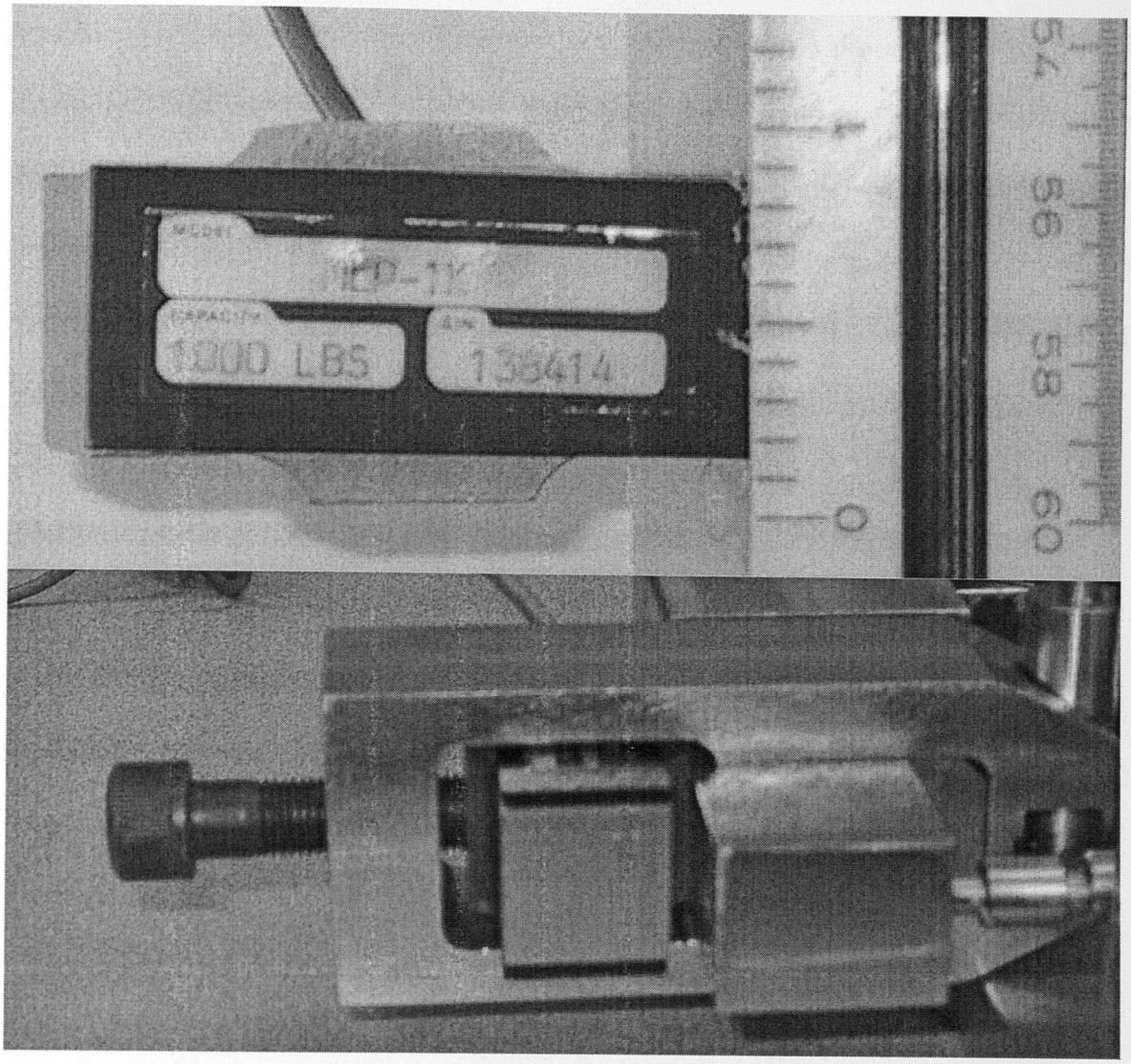

Fig. 19 MLP 1000 lb. load cell (top). Load cell in stage grip (bottom).

These modifications allowed the stage to fit into the chamber, but not with much room to spare. Placing the stage in the chamber takes some adjustment of the door platform after calibration, see the section 3.3 on ESEM stage operating procedures. Once the stage is maneuvered into the chamber it is necessary to obtain an image with a sample in the stage grips inside the chamber. Originally, the grips were designed to hold

samples at the midpoint between the two grip clamps, with a pin sliding through the assembly. This was done for symmetry once again, but proved to be a major flaw in the design. This places the sample too far from the electron beam objective and made it impossible to obtain a focus on the sample. It was an absolute necessity to move the sample location. In figure 20 new pin designs can be seen. The sample is not held between the grips, but above them. Thus allowing for a clear picture to be obtained.

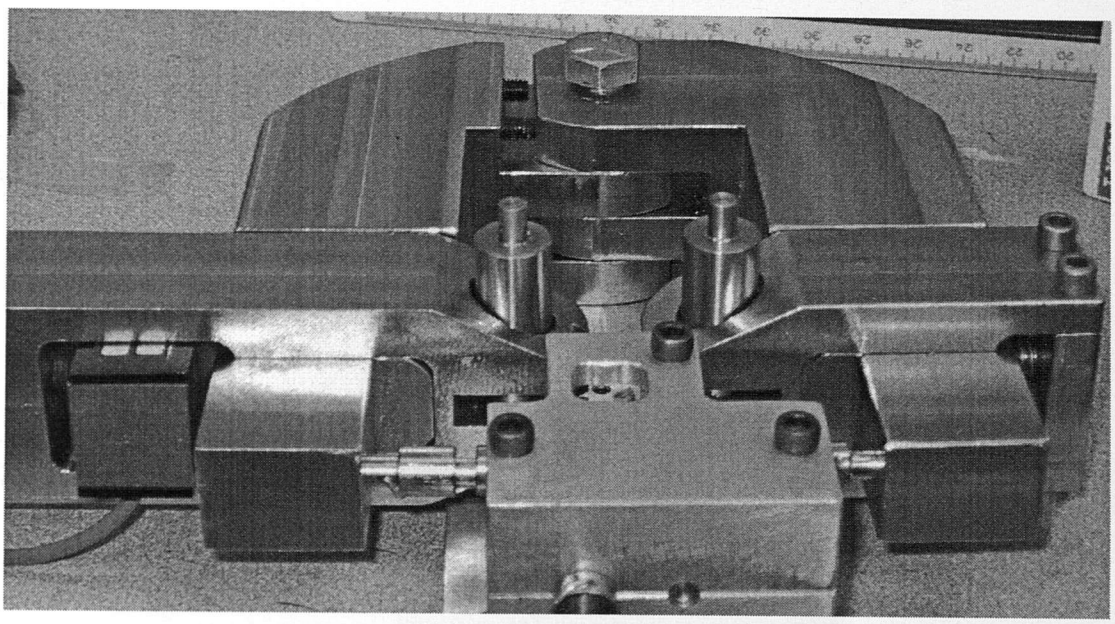

Fig. 20 Modified sample pins.

These new modifications produced pictures from the ESEM of samples under tension. When the ESEM motors were used to drive the screws to open and close the grips of the stage, a new problem arose with the design. The gears are connected to the screws through a small universal coupling. This is an off-the-shelf item made by small parts (Small Parts Num. MJC-125). These miniature universal couplings are held in

place with two 0.035" set screws. These were very difficult to tighten sufficiently. The continually would slip under load. Once they were sufficiently tight to hold a load, the central nylon shaft would fail. The original coupling ends were used to make a new stronger universal joint. A steel shaft was machined to replace the original nylon shaft and some set pins were placed completely through the couplings, to prevent slipping. These can be seen in figure 21. Set pins were also added to the drive shaft universal to prevent any slippage there.

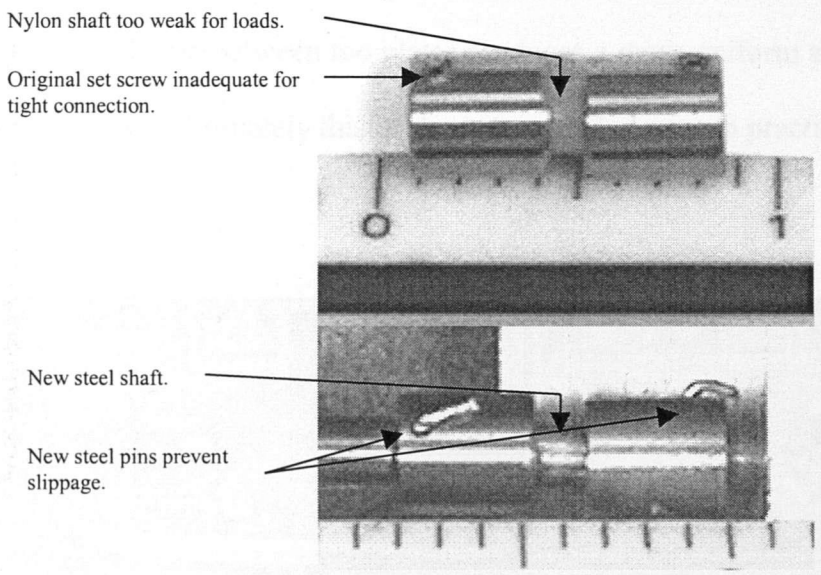

Fig. 21 Original universal coupling (top). Modified universal coupling (bottom).

These improvements proved effective to produce images in the SEM while subjecting samples to tensile loads, but there continued to be problems with the stage. The crack tip location was not stable on the screen due to the materials ductile properties. Preliminary tests using KELF, which has fairly ductile qualities, resulted in

the crack tip wandering out of the field of view. The tensile stage would subject a load to the sample, and indeed the crack tip would open. Due to the plastic deformation of the material around the grip pins the material would also yield around the pins. As the material would not yield around the pins completely symmetrically, it would cause the crack tip to unpredictably move in any direction. New grip pins were redesigned to pinch the material between two plates, see figure 22. This design not only holds the sample much closer to the crack tip, but it also distributes the load more evenly across the material. Holding the sample closer to the crack tip prevents material from yielding in areas away from the crack tip, which results in unstable crack tip displacement. Pinching the sample between too plates produces a more uniform application of force on the sample ends. Ultimately this is closer to what happens in practical situations.

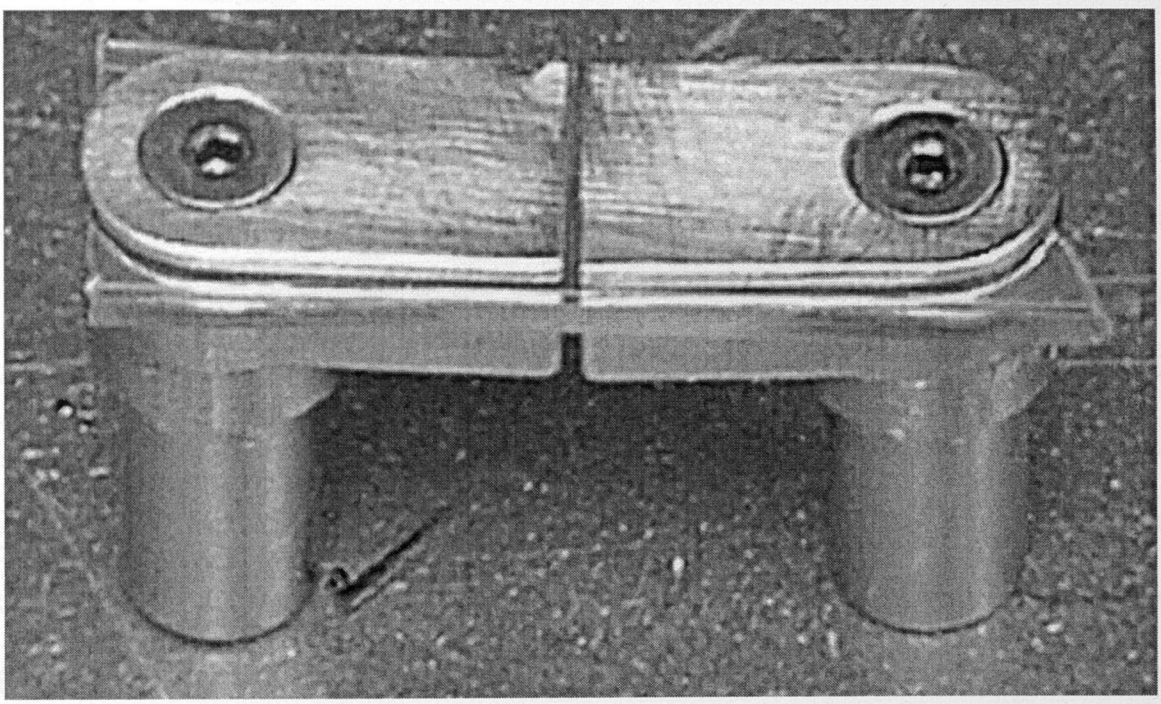

Fig. 22 Redesigned grip pins.

These new pins were machined to press-fit tolerance. This means that they require some force to push them into their respective grip holes and thus minimizing any side to side movement. The new design works well, but not perfectly. Smooth materials like KELF still tend to unpredictably yield away from the crack tip and thus inducing crack tip positional movement. It is recommended that the pinch plate surfaces be burred or roughed, and possibly adding a second set screw to each pin. Hopefully this will aid in gripping the sample ends more firmly.

Another area that needed improvement was the gearbox and universal couplings. These join the gears to the drive screws. The prior improvements proved effective in strengthening the design so that a load could be applied to the material sample. The crack tip placement stability problems still persisted with this design because of the slack between parts in the drive system. There was a small amount of side to side movement of the gears. Bushings were placed around the gears to prevent any movement that may effect the crack tip position.

The modified universal couplings also had similar problems. The steel shaft provided sufficient strength for testing. Combined with the improved set pins, there is no slip while rotating. Unfortunately there was expansion movement between coupling ends and the central steel shaft. The flexibility of the coupling also ultimately limited where the grip movement had to stop. With the current design the total movement of the sample ends was approximately 1/4 inch. This was not enough displacement for effective testing. The goal for the design was to maximize the amount of travel of the grips, making the stage able to test a variety of different materials. The stage as a whole

was size limited by the ESEM chamber doorway. Given the limitation of the overall size of the stage, the maximum rotation of the stage arms is therein limited. With these two limitations a total displacement of one inch not only seemed to be reasonable but attainable. Completely new universal couplings replaced the original ones in an attempt to achieve this. The new couplings provided minimal slack in the connection of the gears to the drive screws and sufficient strength to apply a large load to the samples, see figure 23. The new configuration increased travel of the grips from one quarter of an inch to approximately two-thirds of an inch. Longer drive screw would allow for even more travel. Unfortunately, at larger displacements (½" or more) the stage arm rotation begins to noticeably effect crack tip placement.

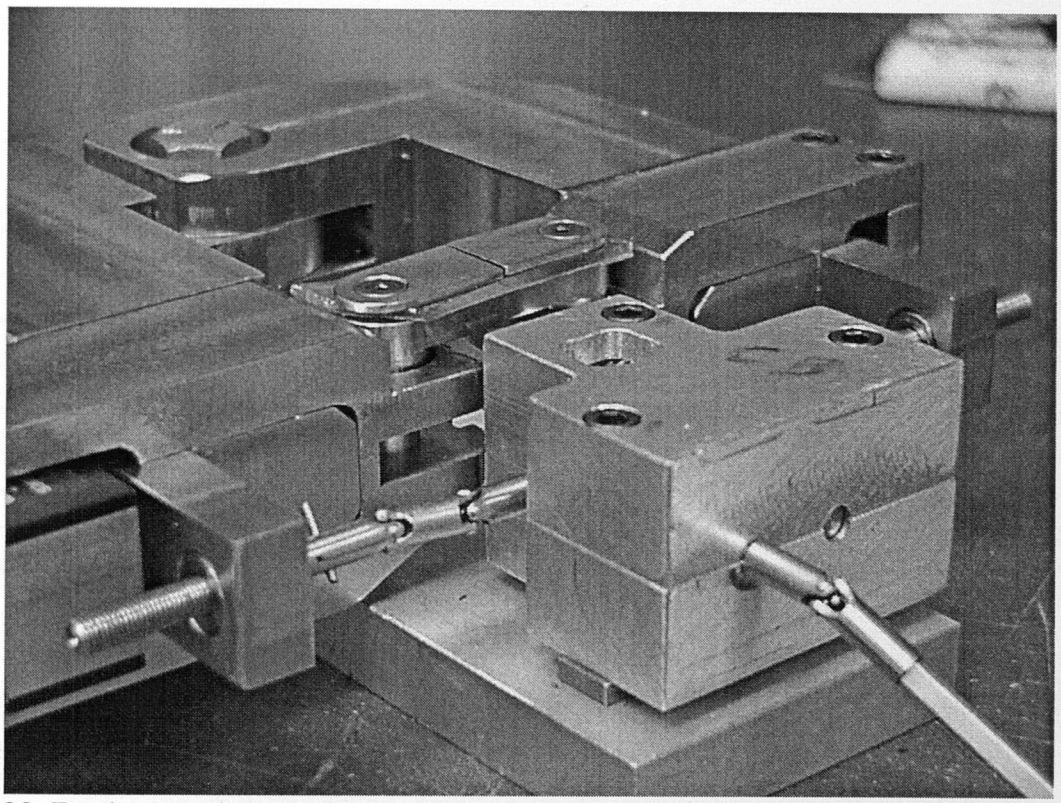

Fig. 23 Revised design of universal couplings.

The ESEM tensile stage works as a part of the ESEM and therefore does not require much setup, only attaching it to the doors' translation platform and motor drive shaft. Conversely, operation of the ESEM is much more labor intensive than optical experiments. Below in table 2 is a list of equipment used in the ESEM experiments. Each piece of equipment is labeled with a Greek letter. Following, figure 24 is a flow chart that shows not only how the equipment is set up, but also how the microscope interacts with the stage, the stage with the sample, and how information is transferred. It is important to note that the ESEM is made of several parts. It is only listed as one piece of equipment in the table, but its different parts are labeled in the flow chart. All parts, however, are labeled α as in the table. This is to show how the microscope is operated and how information is passed to different pieces of equipment. The sample itself does not have a Greek letter and is not found in the table of equipment.

Table 2 ESEM Experiment Equipment

α	Microscope	Electroscan ESEM model E-3
β	Tension Stage	Screw actuated EM tensile stage, (custom made)
δ	Computer	Dell 3800 Inspiron laptop
ε	Control and Edit	Belkin USB VideoBUS II and MGI Video III software
ϕ		Transducer Techniques MLP-1K Load Cell
γ	Load Measurement	Transducer Techniques DPM-3 Digital Panel Mount Meter
		With Analog Output and Serial Data Output (RS-2302)
η		RS-232 to Serial Converter

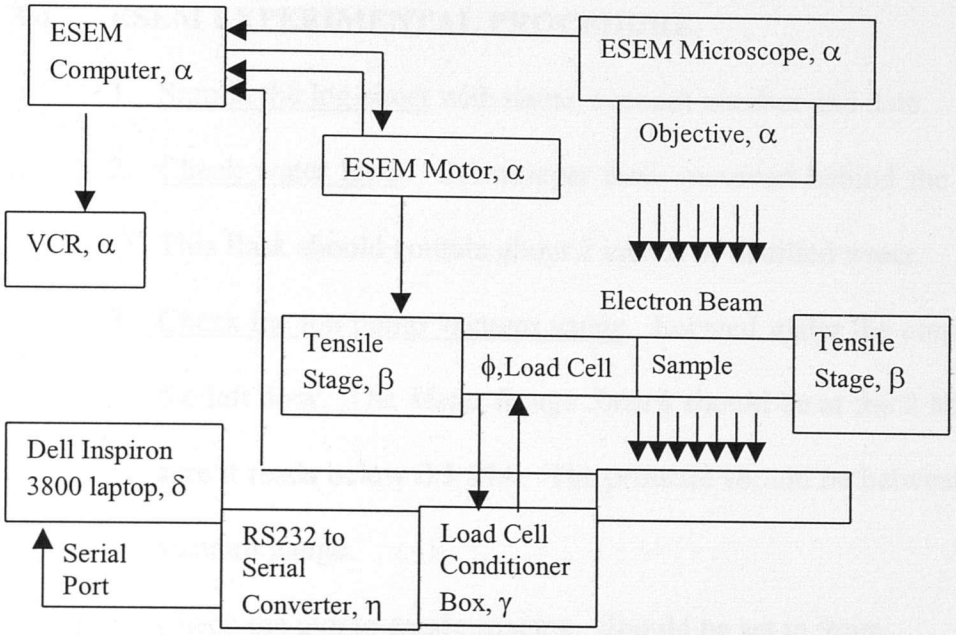

Fig. 24 Flow chart of ESEM experiment (top). ESEM microscope (bottom).

3.4 ESEM EXPERIMENTAL PROCEDURE

1. Sign in the log-sheet with name, account number and date.
2. Check water level. Erlenmeyer flask mounted behind the column console. This flask should contain about 2 inches of distilled water.
3. Check the ion pump vacuum gauge. Located under the console panel behind the left door. The *Meter Range Switch* should be at the 2 MA setting. Make sure it reads below 0.5 MA. The pressure should be between 10 & 10 on the vacuum gauge.
4. Check the gun to anode spacing. Should be set to 9mm.
5. Turn on computer.
6. Turn on console power by pressing green CONSOLE ON button. Turn on accessories; waveform monitor, specimen chamber light, etc...
7. Calibrate the stage. Open Stage Control Window and select CALIBRATE.
8. Set the Z. From the Stage Control Window select the X-Z button and with the joystick or the toggle switch move the stage/ specimen up to about 1-2 mm below the detector. If stage does not move, turn the magnification knob and try again. This is a glitch and is specific to the A&M Electroscan ESEM. Remember this because while using the ESEM it may be needed again. Once the desired Z distance is obtained press the Z SET button. This will prevent the stage from moving any closer to the detector. Press the X-Y button to switch the controls back to the X-axis.
9. Select WET from the Vacuum Control Window.

10. Set the chamber pressure to 5.0 Torr. Press the SET button on the pressure servo control panel and turn knob util it reads 5.0. Press the SET button again to disengage it to the normal "out" position.
11. Heat the electron gun source. Open the Gun Control Window and select HEAT FILAMENT.
12. Select accelerating voltage. From the left Control Window turn on accelerating voltage by clicking on the ON button in the Beam KeV section. Use the middle mouse button to click the single arrow-up button, which will increment the voltage in 5 KeV steps, pausing briefly between steps. Go to 30 KeV and stop there. After the filament is at the set point, (about 3-4 minutes) decrease KeV to desired setting, usually 15 KeV.
13. Obtain an image. Set magnification to ~100X. In the Left Control Window set scan rate to 2.1 sec/fr. Turn the brightness knob until the image is dark to medium gray, then turn the contrast knob clock wise until images appear. Use focus knob to roughly focus the image. You will end up with an image of the test sample (grid) that is partially restricted through the size of the bullet hole.
14. Center the source. For optimum image brightness the filament needs to be centered. Use the three knobs on the top of the column. While watching the image on the monitor, first turn the front knob slightly until the image gets bright and then dark again, then turn the knob back to get the image at its brightest point. Do the same thing with the left rear knob, then again with the

front knob, then with the right rear knob. Rotate between the knobs in this manner until the image is as bright as possible. In the process of turning the knobs the image may get so bright the screen goes white, if this happens turn down the contrast until the image return and continue alignment. There will be a loss of brightness de to instability it will take about 30-40 minutes to stabilize. You may need to repeat this step as you start looking at samples.

15. Center the projection aperture. Adjust the magnification to 5000x or higher. In the left control window adjust SCAN RATE to 2.1 fr./sec or faster. Go into partial field mode by pressing the square P.F. button on the front panel. Find an area with distinctive features and adjust for higher contrast. Focus and stigmate with x and y stigmator knobs to the right of the focus knob. Press the square ALIGN button, on the front panel. The image, which will be live inside the partial field window will be going in and out of focus (aka wobbling) and may be moving in the X, Y or diagonal direction as well. Adjust the aperture alignment knobs in the front center of the column until the image is stable. It will continue to go in and out of focus, but should not be moving side to side.
16. Vent chamber, from the Vacuum Control Window select VENT CHAMBER button. It is important to make sure that the Vent button in the Gun window is not pushed. This will damage the ESEM.
17. Open chamber door, and remove the sample pedestal stage from the doors platform.

18. Move the platform. First make sure the X-Y button is selected in the Stage Control Window, and use the joystick to move the platform to about the 4800μm position.

19. Attach the stage. Make sure that the stage grips are moved all the way in. IF they are not there, turn the drive shaft by hand until they are completely moved in. Then reverse the motion of the shaft one complete turn. First slide the square stage drive shaft into the right ESEM stepper motor drive shaft. Align the two stage base plate holes with the two appropriate two platform connector holes. Place a connection bolt in each hole and tighten with a 3/32 Hex key. See figure 25.

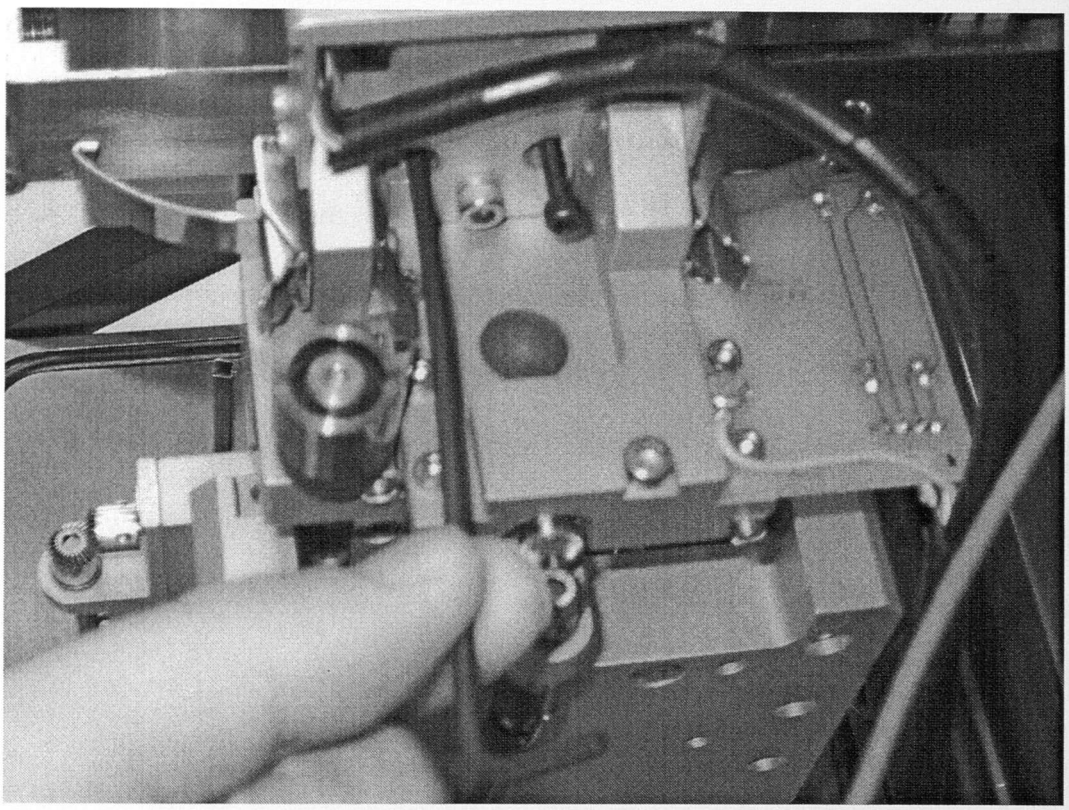

Fig. 25 View from bottom of ESEM platform while attaching stage connector bolts.

20. Connect load cell. The ESEM door has a series of wires that run through the vacuum tight door. Connect the load cell to the correct wire. There are only two connectors that will fit the load cell connector. Only on has four wires running though it, this is the one that should be used. Make sure that the appropriate opposite end is connected to the load cell condition box. The conditioner box will change from reading all 9's to the actual load on the load cell when this is done. Once this is done, make sure that all wires are clear of the door alignment bar that guides the door into the proper position while it is being shut.

21. Test the tensile stage range of motion. In the Stage Control Window, select the TLT button. Normally this controls the motor that drives the tilting operation of the sample pedestal. This is the motor that will control the operation of the opening closing of the stage grips. The window should read 0° or approximately 0°. Hold the joystick in the down position. This will turn the drive shaft and open the grips. Make sure the sample is not connected to the stage at this point, or it will have already been cycled one time when it is viewed in the ESEM. Hold the joystick down until the window readout approaches 1650°. Make sure that the stage can move without problems from 0° to 1650°. This is the range of motion. Do not go above 1650° or below 0°, this will result in damaging the stage or the ESEM. Of course the stage had not rotated 1650°, but this is how it is known when the stage is reaching the limit of its travel. 10° corresponds to on complete

rotation of the drive shaft. Seven rotations of the driveshaft corresponds to on complete rotation of the screw which has 40 threads per inch. Therefore, 280° is representative of 0.1 inch of displacement. Notice that one the joystick is released that there is a small lag in the readout versus when the joystick is actually released. This is important to note because if the joystick is release when the readout is 650°, the motor will actually stop at a position past 650°. The stage is now ready to be used, see figure 26.

Fig. 26 ESEM tensile stage attached to platform.

22. Attach the sample. First attach the sample to the stage grip pins and then place the pins into the grips.
23. Shut the chamber door, and pull a vacuum in the chamber. Select WET in the Vacuum Control Window.
24. Unset the Z. In the Stage Control Window, select the Z set button. This will result in a red lettered warning about the Z-set appearing in this window. Remember this will need to be reset again.
25. Select the X-Y Control in the Stage Control Window.
26. Set the Z. From the Stage Control Window select the X-Z button and with the joystick or the toggle switch move the stage/ specimen up to about 1-2 mm below the detector. If stage does not move, turn the magnification knob and try again. Once the desired Z distance is obtained press the Z SET button. This will prevent the stage from moving any closer to the detector. Press the X-Y button to switch the controls back to the X axis.
27. Obtain an image. Set magnification to ~100X. In the Left Control Window set scan rate to 2.1 sec/fr. Turn the brightness knob until the image is dark to medium gray, then turn the contrast knob clock wise until images appear. Use focus knob to roughly focus the image. You will end up with an image of the sample.
28. Find the edge of the sample. First, turn down the brightness and move the joystick to position the bullet near the edge of the sample. This can be done by watching the image on the screen and also through the chamber window.

Once the edge of the sample is found move the stage until the crack tip is found. It will be necessary to readjust the brightness once the field of view is away from the sample edge.

29. Adjust the controls. From the Left Control window it may be a good idea to adjust some of the settings to optimize the view. Usually the condenser works well around 45-50, Beam around 15 KeV, and Vacuum around 5 Torr.
30. Prepare the video tape. Place a VHS tape in the VCR for recording the session. Once the record button is pushed what ever is being done will be recorded. It is not necessary to record the whole session, but it is best to have the tape ready for immediate use.
31. Video Frame rate. Typically the slower the frame rate the clearer the image is on screen. Unfortunately this can slow down the adjustment process when at slow frame rates. 2.1 fr/sec or sec/fr is usually a good speed for adjusting the image and focusing. If a still picture is taken it might be a good idea to slow the rate down to 4.3 sec/fr to see about what it will look like when the still is taken. The image will be much clearer this way. This rate is much too slow for video of the tensile test. Once the tensile test is started a frame rate of 2.1 or 4.3 fr/sec will probably yield the best results.
32. Start the tensile test. Once the image is optimized and the tape is prepared, it is time to start the test. Select the TLT button in the Stage Control Window. Moving the joystick down will open the grips while up will close them. In this mode left and right movement of the joystick will still move the sample

to the left and right. When the material yields sometimes the crack tip will tend to wander on screen. If the portion of the sample that is under examination moves off the top or the bottom of the screen it is necessary to stop the tensile test, select X-Y button in the Stage Control Window, reposition the sample, reselect the TLT function, and restart the test from where it was stopped.

33. Vent chamber when finished. After the test has been completed choose the Vent Chamber button in the Vacuum Control Window.
34. Remove Sample. If another sample is to be tested, place the sample in the grips and return to step 23. If no other samples are to be tested proceed to step 35.
35. Set pressure to 10 Torr and lower contrast.
36. Choose Wet from the Vacuum Control Window.
37. Set pressure to 5 Torr when wetting is complete.
38. Select STANDBY Vacuum from Vacuum Control Window.
39. Select Cool Filament from the Gun Control Window. This will take about 5 minutes for the reading in the window to display zero.
40. Turn console OFF and the waveform monitor and any other accessories.
41. Sing out of logbook.

Optimizing the image in WET mode:

- Flush the chamber. Since the specimen chamber was originally at atmospheric pressure, it is necessary to flush out the air in the chamber and replace it with water vapor. Air in the chamber may give an unstable image, which would appear as horizontal "streaking".
- Use the FLOOD button on the pressure servo control panel to increase the chamber pressure. Set the pressure to about 1.5-2.0 Torr and press and hold the FLOOD button and release the button when the pressure reaches 7-8 Torr. Do this three times.

  In the process of floding the chamber notice the image on the screen. When the image reaches its brightest, take note of the Torr reading and this should be the best operating pressure for the sample. The default setting of 5 Torr can also be used.
- Adjust contrast and brightness. Image quality can be improved by varying the levels or contrast and brightness. There is no set formula for a optimal image quality, it requires varying both levels and finding the best combination.
- Center the source again. See step number 14. As the filament warms up there may be some movement and therefore re-setting the alignment can improve image quality.

3.5 CALIBRATION OF MOTORS

For the ESEM tests, the calibration is performed with a caliper micrometer. Each rotation of the drive shaft of the tensile stage is equivalent to a certain amount of travel of the grips of the stage. This travel is measured with the micrometer. As the computer rotates the drive shaft of the grips, the rotations of the shaft are counted, thus producing strain data for the tests. Therefore even though the degrees of rotation of the TLT function on the ESEM was not originally designed for this stage, it can be directly related to the expansion of the grips.

As stated in chapter II the load cell is highly accurate. The same load cell is used in both experiments. The manufacturing company, Transducer Techniques, publishes the calibration and accuracy of the loadcells. It has nonrepeatability of 0.05%, Hysteresis of 0.1% and a zero balance of 1%

CHAPTER IV

RESULTS

The first step in the analysis of the data is digitizing the video. Video capture is relatively simple. It only consists of installing the videobus driver and configuring the video editing software to capture the video. The hardware comes with detailed instructions for installation and configuration for capture and will not be reviewed in this chapter.

Once the equipment is installed and configured each experiment is played on either the Handicam or VCR. The entire experiment is converted into a digital video through the videobus. In the case of quasi-static experiments, where individual test are hours in length, the video may need to be sampled at one frame per second or more to reduce the size of the file. Video files are very memory intensive and even short videos can require hundreds of megabytes (MB) in space. A system with 256 MB of RAM or more is recommended, as well as a very large hard drive. The larger the hard drive the better. For example, a one-minute 16-bit color video that is 320x240 pixels in dimension is nearly 250 MB in size. For an extensive study of a multitude of samples, forty or fifty gigabytes (GB) of available hard drive space would not be excessive. In fact, a larger hard drive is recommended, along with a CD burner for cheap long-term file storage.

In the case of the optical tests, the footage is recorded on 8mm videotape. This is played in the VTR mode of the Handicam utilizing its S-video output port. In the case of the ESEM experiments, the raw footage is recorded on a VHS tape and output

through either its S-video output or RCA output. In either case, the output is connected to a Belkin USB videobus II devise for digitizing. The Belkin videobus only converts the signal to a digital format that can be accepted by the computer. A commercial software is required to capture and edit the video.

Suitable software for analyzing these experiments requires only a few features. Of course more features may be used to optimize images, but the software must be able to capture the video from the videobus devise first and foremost. If the video cannot be captured, no analysis can be performed. For the development of this experiment the video was captured and saved in either .MPG or .AVI format. This format has adequate picture quality and file size per second of video. Idealistically file size would not be an issue and a full digital video of the exact signal would be made. This is very computer memory intensive and not needed for this developmental stage. The other requirement of the software is the ability to review the digital video frame by frame and capture selected frames at will. The single frame needs to be captured as a typical digital picture format like .JPG, .BMP, .GIF, .TIF, etc.

With regards to what is done in editing, the process is rather simple. Most commercially available video editing software will have more options than are needed for this experiment. The Belkin Videobus comes with MGI Videowave III software for editing. This software is the user-friendliest. Conversely, it is also the most limited. Specifically, picture dimensions are limited during the capture process. This limits the quality of the analysis, but both video capture and frame selection can be performed

with one software. Neither the Videowave III nor the Photosuite III software (which also comes with the videobus) will perform the image analysis.

Ulead Mediastudio Pro Video Edition Version 5.0 and Adobe Premier 5.1 were both examined also. These two video editors are more advanced than the MGI. The learning curve was much higher due to the massive amount of options that are available and not needed for this experiment. Interestingly enough, the Ulead software did an excellent job of video capture but it would not easily allow for isolating single frames. It would also capture the video with larger dimensions than the MGI software. Video was captured at 600 x 480 pixels versus MGI's 300 x240. Conversely, the Adobe software would not easily capture video from the videobus hardware, but it would easily select single frames for analysis. Unfortunately, neither of these software's had the image editing properties needed for final analysis.

Once the video is digitized it is necessary to review the video frame by frame, paying attention to fibril development. The objective is to locate the exact frame in the video where a single fibril fails. Then, select the frame prior to this moment and extract it. This extracted image is used for analysis. This moment shows the critical fibril length and diameter.

A second software is required for the analysis of the selected single frames. Most commercial photo editing software is adequately capable of editing. Only two functions are essential. One, the picture needs to be marked with a line to identify where and how long the fibril in question is. This helps to differentiate where fibrils start and end when the image is magnified immensely. Thus, the second requirement is

the ability to magnify the digital image to the point where single pixels can be identified and counted. PaintShop Pro 6 was exclusively used to do this. Much like the video editing software, PaintShop has more functions than are needed. PaintShop Pro 6 is user-friendly in magnifying and marking the pictures. Adobe PhotoShop 5.5 is also available commercially but was not thoroughly examined. For more intricate material studies software specifically suited to scientific imaging is highly recommended.

4.1 IMAGE ANALYSIS

After the video is digitized and single frames have been selected, each selected frame must be analyzed. This was done in PaintShop Pro 6 and MS Excel. Each fibril is measured in length and width and located relative to the outer dimensions of the sample. To do this, the selected images are opened in the photo editing software. The length of the fibril is marked with a clearly defined line. Next, the image is magnified to determine the end pixels of this line. In PaintShop Pro each pixel is assigned an (X, Y) coordinate. Using simple geometry these coordinates determine the pixel length of the fibril, see figure 27.

It is necessary to have an image of an object of known length taken from the exact same perspective as the experiment. An engineering ruler works well for this. The length scale image has to be taken with the exact same camera settings and position to ensure that when the analysis of the fibrils is performed the length scale image and the fibril image will have gone through the exact same magnification. The ruler image determines the length of one pixel. The selected image determines the number of pixels in the length of a singular fibril, and together the actual length is determined.

Fibril length $= \sqrt{(X_2 - X_1)^2 - (Y_2 - Y_1)^2}$

Actual Length = Pixel Length X Fibril Length

Fibril	2	
Real Time	12:26:59	
Elapse Time	0:11:51	
Coordinates	X	Y
Fibril Left End	119	178
Fibril Right End	229	178
Fibril Top	215	176
Fibril Bottom	215	181
	Pixels	Inches
Fibril Breaking length	110	0.21875
Fibril Breaking Width	5	0.0099432

Fig. 27 Analysis of rubber cement cohesive zone frame.

This kind of analysis is completed for each fibril. Then, a statistical analysis is performed for the experiment as a whole. This will determine the average critical breaking length and diameter along with their standard deviation. It is also important to know where the fibril is located with respect to the sample. This will be needed to determine the strain rate each fibril is experiencing. Strain rate is used to calculate the traction and is explained in the following section.

4.2 MICROMECHANICAL APPLICATION

The micromechanical analysis has been completed on the asphalt because there are no data currently available about the relaxation modulus of rubber cement. The rubber cement experiments were only used to develop the video capture, editing and analysis techniques. The video images are used to determine the location of the fibril with respect to the overall size of the sample. The experiment was designed so that a

known velocity is applied to the movement of the sample holes. Knowing the velocity of that point exactly, the time over which the experiment is performed and the geometry, the angular velocity or rate of rotation of the sample is also known. See figure 28 and equations 4, 5 and 6 for details. Because the sample sides are being rotated at a known rate, the tangential velocity of any point is a function of the radius from the hinge point. Therefore, the strain rate of each fibril can be determined by its location.

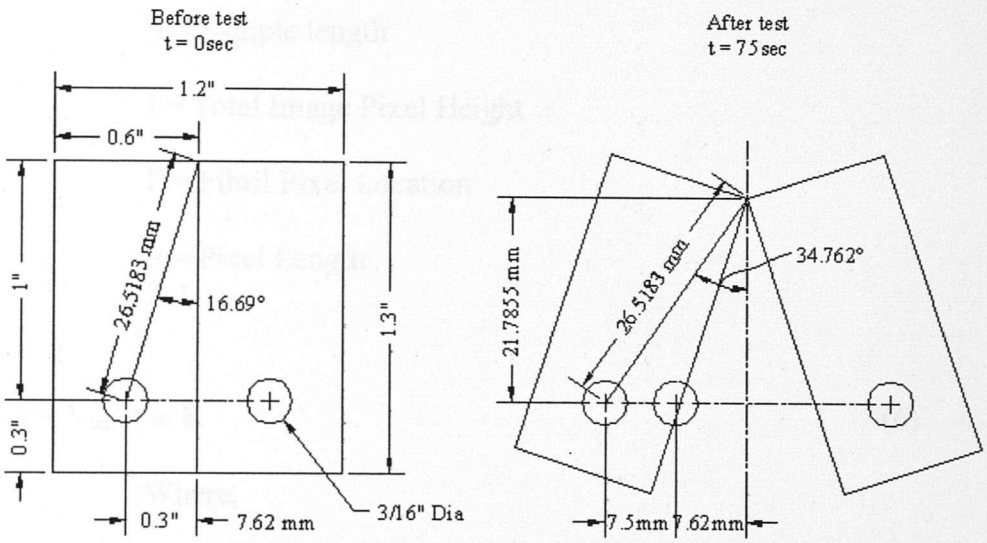

Fig. 28 Compact tension sample before and after test.

$$\text{Angular Velocity} = \omega = \frac{\theta_{end} - \theta_{start}}{\Delta time} = \frac{34.762° - 16.69°}{75\,\text{sec.}} = 0.240838\,{}^{\circ}/_{Sec.} = 4.2034\,{}^{Rad.}/_{Sec.} \qquad (4)$$

Using the fibril found in the image in figure 27 as an example, the radius of rotation is determined by pixel location. That image is 320 pixels wide and 240 pixels

high, with pixel (0,0) being in the upper left-hand corner. The fibril is located at a pixel level of 178 and the whole specimen is 1.3 inches in length. The video camera is aligned so that the 240th pixel level is the very farthest edge sample from the hinge point. Equation 5 is used to calculate the distance from the hinge point, and equation 6 is used to calculate tangential velocity or strain rate.

$$R = S - (I-F)P \tag{5}$$

Where,

R = Radial Distance from Hinge to Fibril

S = Sample length

I = Total Image Pixel Height

F = Fibril Pixel Location

P = Pixel Length

$$\dot{\delta} = V_{tan} = \omega R \tag{6}$$

Where,

$\dot{\delta}$ = Strain Rate

V = Tangential Velocity

ω = Angular Velcity

R = Radial Distance from Hinge to Fibril

Before the traction applied to a fibril can be calculated, the viscoelastic material properties need to be known. Asphalt material tests are readily available and were used for the traction calculations. From material tests, the shear relaxation modulus was measured and approximated in a Prony series, see equation 7.

$$E(t) = E_{\infty} + \sum_{1}^{i} E_i e^{-t/\eta_i} \tag{7}$$

G_i, E_i, ρ_i, and η_i are all material properties. All unites of G were originally measured in Pascal's (PA) and are found in table 3, but were converted to pounds per square inch (PSI) for E_i in table 4. The traction equation to be used later uses a uniaxial modulus prony series approximation and thus E_i and η_i need to be determined.

Table 3 Shear Relaxation Modulus Properties in Pa

$G_1 = 26133234.05$	$G_6 = 19075.52605$	$\rho_1 = 0.00157484$	$\rho_6 = 65.77483389$
$G_2 = 9109248.397$	$G_7 = 3013.443065$	$\rho_2 = 0.016405528$	$\rho_7 = 643.5327398$
$G_3 = 3873988.606$	$G_8 = 476.4126453$	$\rho_3 = 0.099510179$	$\rho_8 = 6494.899371$
$G_4 = 742192.5312$	$G_9 = 89.95077602$	$\rho_4 = 0.735571193$	$\rho_9 = 81020.88289$
$G_5 = 118638.9335$	$G_\infty = 43.51727935$	$\rho_5 = 6.770533599$	

We can use the following relationship to obtain uniaxial modulus (E_i) from shear relaxation modulus (G_i) when we also know that Poisson's ratio (ν) is 0.45 with equation 7.

$$E_i = 2G(1+\nu) \tag{8}$$

While η is determined through equation 9.

$$\eta = \rho/G \tag{9}$$

Table 4 Uniaxial Modulus Properties in PSI

$E_1 = 1.10 \times 10^{+04}$	$E_6 = 8.02 \times 10^{+00}$	$\eta_1 = 2.08 \times 10^{-11}$	$\eta_6 = 1.19 \times 10^{-03}$
$E_2 = 3.83 \times 10^{+03}$	$E_7 = 1.27 \times 10^{+00}$	$\eta_2 = 6.21 \times 10^{-10}$	$\eta_7 = 7.63 \times 10^{-02}$
$E_3 = 1.63 \times 10^{+03}$	$E_8 = 2.00 \times 10^{-01}$	$\eta_3 = 8.86 \times 10^{-9}$	$\eta_8 = 4.70 \times 10^{+00}$
$E_4 = 3.12 \times 10^{+02}$	$E_9 = 3.78 \times 10^{-02}$	$\eta_4 = 3.42 \times 10^{-07}$	$\eta_9 = 3.11 \times 10^{+02}$
$E_5 = 4.99 \times 10^{+01}$	$E_\infty = 126.2011$	$\eta_5 = 1.97 \times 10^{-05}$	

Now that the material properties of the bulk are known we will assume that the modulus of the bulk remains the same in the individual fibrils. Therefore, the prony series approximation can be applied to a traction-displacement equation for a single fibril. Traction is a function of material properties, strain rate, and time; see equation 1.

$$T_i(t) = \frac{1}{\lambda}\frac{\delta_i}{\delta_i^*}[1-\alpha_1(t)]\left[\int_0^t E_{cz}(t-\tau)\frac{\partial\lambda}{\partial\tau}d\tau\right] \text{ (no sum on i)} \qquad (1)$$

Because these tests are done in pure mode one failure without damage, the equation simplifies.

$$T(t) = \int_0^t E_{cz}(t-\tau)\frac{\partial\delta}{\partial\tau}d\tau \qquad (10)$$

Each fibril undergoes a constant strain rate, which simplifies the equation even further to:

$$T(t) = \dot{\delta}\int_0^t E_{cz}(t-\tau)d\tau \qquad (11)$$

A prony series approximation is used for the material properties, resulting in equation 12.

$$T(t) = \dot{\delta} \int_0^t \left(E_\infty + \sum_1^9 E_i e^{-t/\tau} \right) d\tau \tag{12}$$

This is solved by u-substitution where we let u = t-τ and du = -dτ.

$$T(t) = \dot{\delta} E_\infty t + \dot{\delta} \int_0^t -(\sum_1^9 E_i e^{-E_i/\eta_i}) u du \tag{13}$$

which is simplified to equation 14.

$$T(t) = \dot{\delta} E_\infty t + \dot{\delta} \int_0^t (\sum_1^9 E_i e^{-E_i/\eta_i}) u du \tag{14}$$

The traction-displacement equation is finally solved through integration, see 15.

$$T(t) = \dot{\delta} E_\infty t + \dot{\delta} \left[\sum_1^9 \eta_i \left(1 - e^{-E_i/\eta_i} \right) \right]_0^t \tag{15}$$

In turn, one experiment determines the resulting failure traction applied to each of the various fibrils and their associated strain rates.

4.3 DATA

Rubber cement data was only used for the initial development of the image analysis. Figures 29-36 are an example of the data from one rubber cement compact tension test.

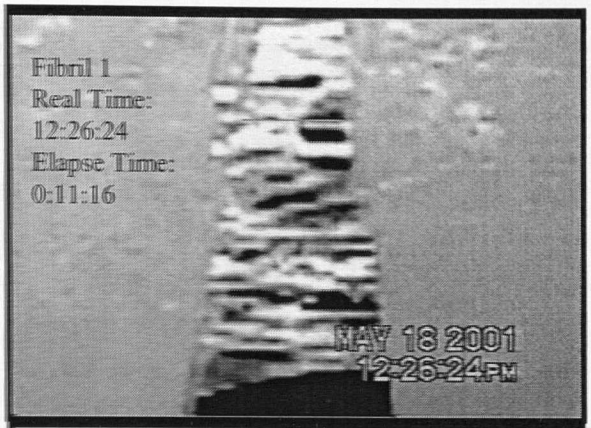

Coordinates	X	Y
Fibril Left End	143	63
Fibril Right End	208	63
Fibril Top	215	176
Fibril Bottom	215	181
	Pixels	inches
Fibril Breaking length	65	0.1292614
Fibril Breaking Width	5	0.0099432

Fig. 29 Rubber cement image 1.

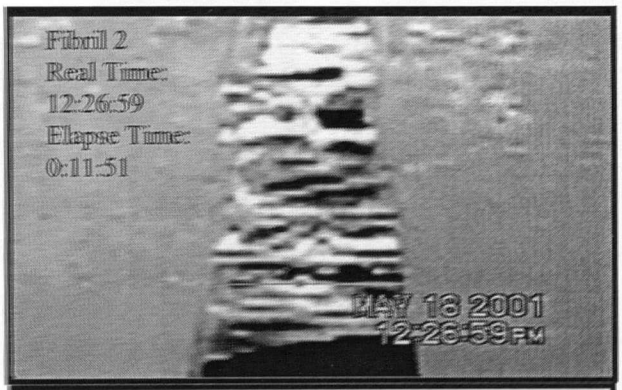

Coordinates	X	Y
Fibril Left End	119	178
Fibril Right End	229	178
Fibril Top	215	176
Fibril Bottom	215	181
	Pixels	inches
Fibril Breaking length	110	0.21875
Fibril Breaking Width	5	0.0099432

Fig. 30 Rubber cement image 2.

Fibril	3	
Real Time	12:30:20	
Elapse Time	0:15:12	
Coordinates	X	Y
Fibril Left End	106	170
Fibril Right End	236	131
Fibril Top	167	153
Fibril Bottom	167	158
	pixels	inches
Fibril Breaking length	135.724	0.2699057
Fibril Breaking Width	5	0.0099432

Fibril	4	
Real Time	12:31:35	
Elapse Time	0:16:27	
Coordinates	X	Y
Fibril Left End	109	122
Fibril Right End	232	103
Fibril Top	176	112
Fibril Bottom	176	117
	pixels	inches
Fibril Breaking length	124.4588	0.2475034
Fibril Breaking Width	5	0.0099432

Fibril	5	
Real Time	12:31:35	
Elapse Time	0:16:27	
Coordinates	X	Y
Fibril Left End	108	120
Fibril Right End	234	107
Fibril Top	176	112
Fibril Bottom	176	117
	pixels	inches
Fibril Breaking length	126.6689	0.2518983
Fibril Breaking Width	5	0.0099432

Fibril	6	
Real Time	12:31:35	
Elapse Time	0:16:27	
Coordinates	X	Y
Fibril Left End	94	198
Fibril Right End	255	186
Fibril Top	194	191
Fibril Bottom	194	196
	pixels	inches
Fibril Breaking length	161.4466	0.3210586
Fibril Breaking Width	5	0.0099432

Fig. 31 Rubber cement images 3-6.

Fibril	7	
Real Time	12:32:20	
Elapse Time	0:17:12	
Coordinates	X	Y
Fibril Left End	119	105
Fibril Right End	235	109
Fibril Top	189	104
Fibril Bottom	189	110
	pixels	inches
Fibril Breaking length	116.0689	0.2308189
Fibril Breaking Width	6	0.0119318

Fibril	8	
Real Time	12:32:45	
Elapse Time	0:17:37	
Coordinates	X	Y
Fibril Left End	106	139
Fibril Right End	245	139
Fibril Top	175	139
Fibril Bottom	175	145
	pixels	inches
Fibril Breaking length	139	0.2764205
Fibril Breaking Width	6	0.0119318

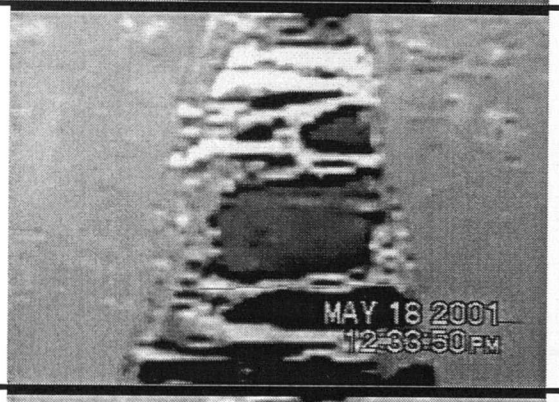

Fibril	9	
Real Time	12:33:50	
Elapse Time	0:18:42	
Coordinates	X	Y
Fibril Left End	93	179
Fibril Right End	259	174
Fibril Top	195	176
Fibril Bottom	195	179
	pixels	inches
Fibril Breaking length	166.0753	0.3302633
Fibril Breaking Width	3	0.0059659

Fibril	10	
Real Time	12:33:50	
Elapse Time	0:18:42	
Coordinates	X	Y
Fibril Left End	78	221
Fibril Right End	269	213
Fibril Top	139	221
Fibril Bottom	139	225
	pixels	inches
Fibril Breaking length	191.1675	0.3801626
Fibril Breaking Width	4	0.0079545

Fig. 32 Rubber cement images 7-10.

Fibril	11	
Real Time	12:34:30	
Elapse Time	0:19:22	
Coordinates	X	Y
Fibril Left End	116	123
Fibril Right End	248	127
Fibril Top	195	125
Fibril Bottom	195	128
	pixels	Inches
Fibril Breaking length	132.1	0.26262
Fibril Breaking Width	3	0.005966

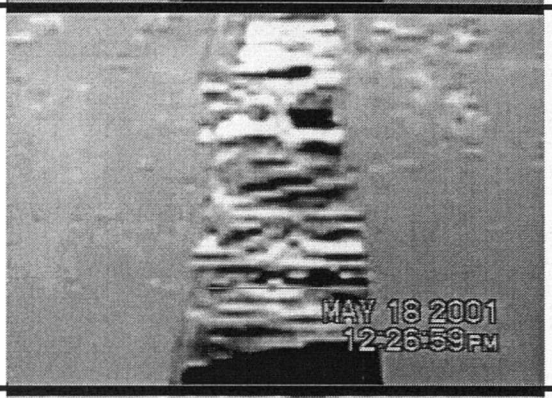

Fibril	12	
Real Time	12:34:30	
Elapse Time	0:19:22	
Coordinates	X	Y
Fibril Left End	99	180
Fibril Right End	259	170
Fibril Top	182	172
Fibril Bottom	182	177
	pixels	inches
Fibril Breaking length	160.3	0.318803
Fibril Breaking Width	5	0.009943

Fibril	13	
Real Time	12:35:16	
Elapse Time	0:20:08	
Coordinates	X	Y
Fibril Left End	106	106
Fibril Right End	248	106
Fibril Top	192	103
Fibril Bottom	192	108
	pixels	inches
Fibril Breaking length	142	0.282386
Fibril Breaking Width	5	0.009943

Fibril	14	
Real Time	12:38:11	
Elapse Time	0:23:03	
Coordinates	X	Y
Fibril Left End	107	65
Fibril Right End	242	56
Fibril Top	172	60
Fibril Bottom	176	64
	pixels	inches
Fibril Breaking length	135.3	0.269062
Fibril Breaking Width	5.7	0.011249

Fig. 33 Rubber cement images 11-14.

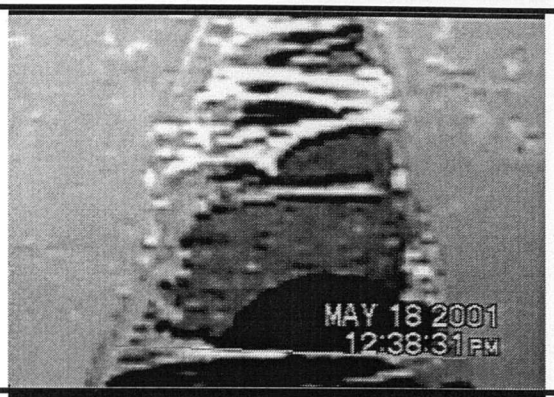

Fibril	15	
Real Time	12:38:31	
Elapse Time	0:23:23	
Coordinates	X	Y
Fibril Left End	68	213
Fibril Right End	290	220
Fibril Top	209	217
Fibril Bottom	209	220
	pixels	inches
Fibril Breaking length	222.1	0.441697
Fibril Breaking Width	3	0.005966

Fibril	16	
Real Time	12:39:36	
Elapse Time	0:24:28	
Coordinates	X	Y
Fibril Left End	122	36
Fibril Right End	236	31
Fibril Top	194	32
Fibril Bottom	194	36
	pixels	inches
Fibril Breaking length	114.1	0.226922
Fibril Breaking Width	4	0.007955

Fibril	17	
Real Time	12:40:06	
Elapse Time	0:24:58	
Coordinates	X	Y
Fibril Left End	99	81
Fibril Right End	254	70
Fibril Top	165	79
Fibril Bottom	165	82
	pixels	inches
Fibril Breaking length	155.4	0.309014
Fibril Breaking Width	3	0.005966

Fibril	18	
Real Time	12:40:47	
Elapse Time	0:25:39	
Coordinates	X	Y
Fibril Left End	115	57
Fibril Right End	250	62
Fibril Top	204	60
Fibril Bottom	204	64
	pixels	inches
Fibril Breaking length	135.1	0.26865
Fibril Breaking Width	4	0.007955

Fig. 34 Rubber cement images 15-18.

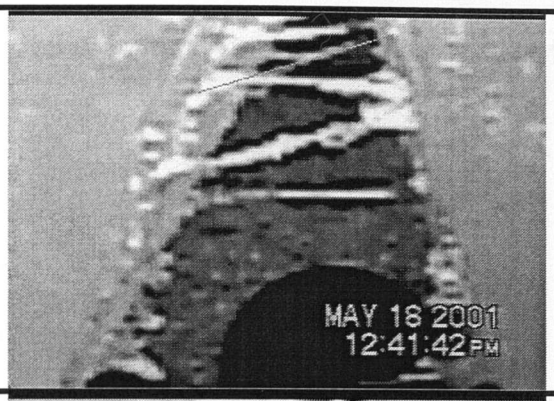

Fibril	19	
Real Time	12:41:42	
Elapse Time	0:26:34	
Coordinates	X	Y
Fibril Left End	120	51
Fibril Right End	244	13
Fibril Top	178	33
Fibril Bottom	180	36
	pixels	inches
Fibril Breaking length	129.7	0.25791
Fibril Breaking Width	3.6	0.00717

Fibril	20	
Real Time	12:42:47	
Elapse Time	0:27:39	
Coordinates	X	Y
Fibril Left End	99	122
Fibril Right End	265	115
Fibril Top	192	119
Fibril Bottom	192	124
	pixels	inches
Fibril Breaking length	166.1	0.330407
Fibril Breaking Width	5	0.009943

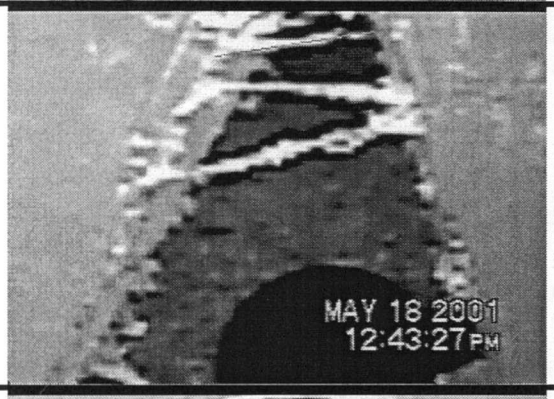

Fibril	21	
Real Time	12:43:27	
Elapse Time	0:28:19	
Coordinates	X	Y
Fibril Left End	131	31
Fibril Right End	238	14
Fibril Top	184	20
Fibril Bottom	184	25
	pixels	inches
Fibril Breaking length	108.3	0.215453
Fibril Breaking Width	5	0.009943

Fibril	22	
Real Time	12:45:18	
Elapse Time	0:30:10	
Coordinates	X	Y
Fibril Left End	114	54
Fibril Right End	259	59
Fibril Top	196	56
Fibril Bottom	196	60
	pixels	inches
Fibril Breaking length	145.1	0.288524
Fibril Breaking Width	4	0.007955

Fig. 35 Rubber cement images 19-22.

Fibril	23	
Real Time	12:49:13	
Elapse Time	0:34:05	
Coordinates	X	Y
Fibril Left End	59	123
Fibril Right End	286	77
Fibril Top	151	103
Fibril Bottom	151	108
	pixels	inches
Fibril Breaking length	231.6	0.460596
Fibril Breaking Width	5	0.009943

Fibril	24	
Real Time	12:53:54	
Elapse Time	0:38:46	
Coordinates	X	Y
Fibril Left End	86	38
Fibril Right End	205	8
Fibril Top	221	21
Fibril Bottom	221	26
	pixels	inches
Fibril Breaking length	122.7	0.244052
Fibril Breaking Width	5	0.009943

Fig. 36 Rubber cement images 23 & 34.

For the rubber cement test it was determined that the average critical fibril length was 0.284672 inches with a standard deviation of 0.07151. While the average critical fibril breaking width is 0.009053 inches with a standard deviation of 0.001834. Due to the lack of material properties for rubber cement no analysis was performed.

After the success of the rubber cement tests, the same procedures were applied to asphalt binder. The viscous nature of the asphalt resulted in develop a cohesive zone larger than could be tested with this equipment. A limestone-reinforced asphalt has a much smaller cohesive zone and was used for this test, see figures 37-49.

AAM-1 Asphalt binder with 25% limestone, Test 2

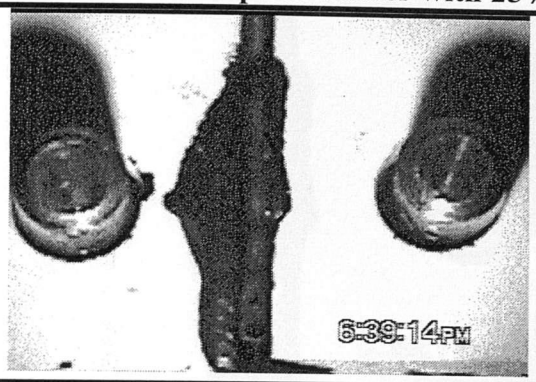

Fibril	1	
Real Time	6:39:16	
Elapse Time	0:00:09	
Coordinates	X	Y
Fibril Left End	144	217
Fibril Right End	154	217
Fibril Top	151	216
Fibril Bottom	151	219

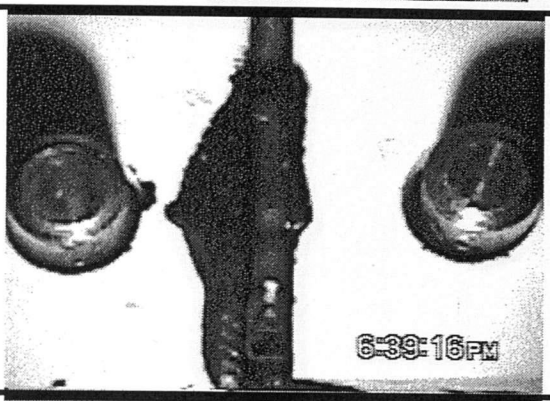

Fibril	2,3,4	
Real Time	6:39:16	
Elapse Time	0:00:09	
Coordinates	X	Y
Fibril Left End	148	184
Fibril Right End	155	184
Fibril Top	152	184
Fibril Bottom	152	186

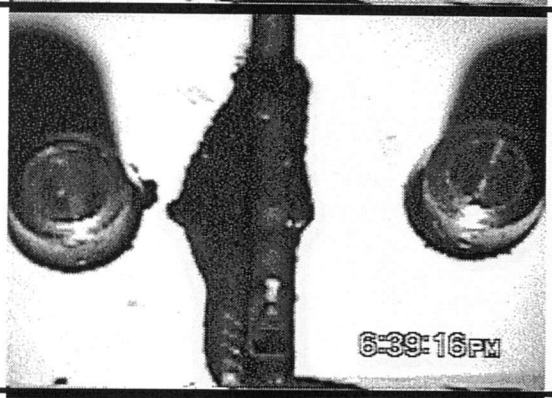

Fibril	3	
Real Time	6:39:16	
Elapse Time	0:00:09	
Coordinates	X	Y
Fibril Left End	145	201
Fibril Right End	155	201
Fibril Top	153	199
Fibril Bottom	153	201

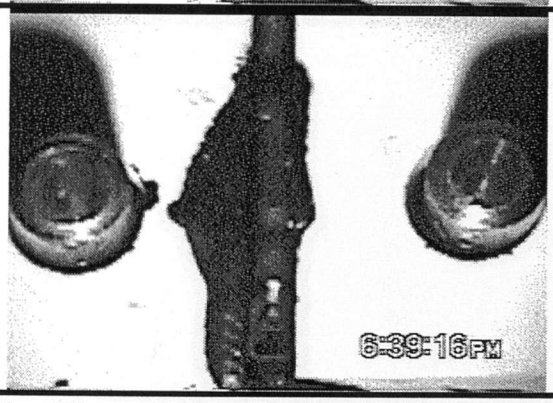

Fibril	4	
Real Time	6:39:16	
Elapse Time	0:00:09	
Coordinates	X	Y
Fibril Left End	145	218
Fibril Right End	158	218
Fibril Top	152	216
Fibril Bottom	152	219

Fig. 37 Asphalt with limestone test 2 images 1-4.

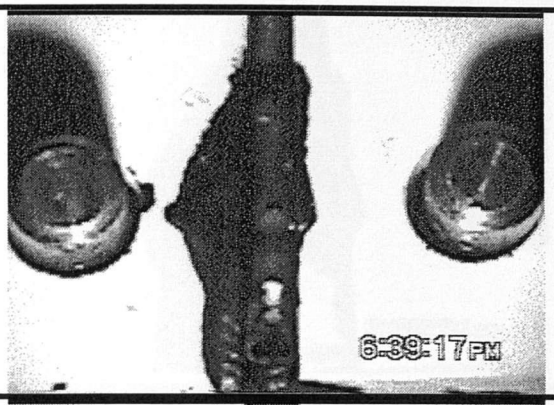

Fibril	5	
Real Time	6:39:17	
Elapse Time	0:00:10	
Coordinates	X	Y
Fibril Left End	145	185
Fibril Right End	157	185
Fibril Top	152	184
Fibril Bottom	152	185

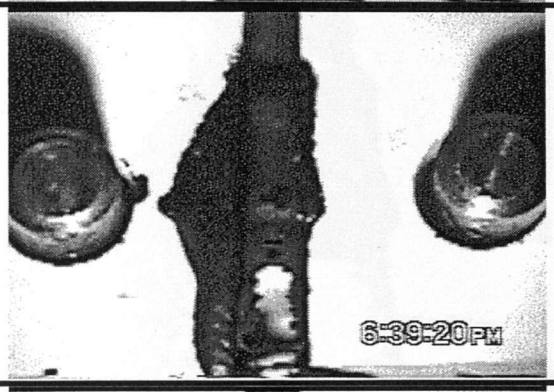

Fibril	6	
Real Time	6:39:20	
Elapse Time	0:00:13	
Coordinates	X	Y
Fibril Left End	145	154
Fibril Right End	157	155
Fibril Top	153	153
Fibril Bottom	153	157

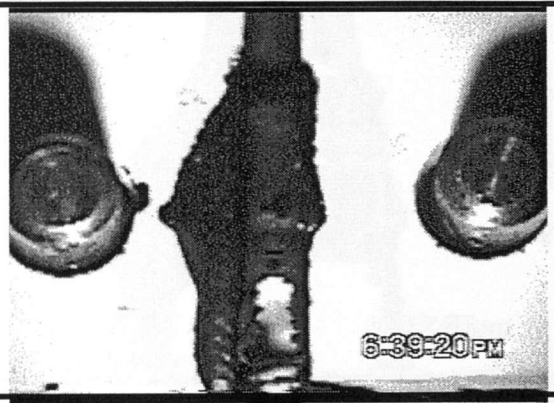

Fibril	7	
Real Time	6:39:20	
Elapse Time	0:00:13	
Coordinates	X	Y
Fibril Left End	144	164
Fibril Right End	158	164
Fibril Top	152	162
Fibril Bottom	152	165

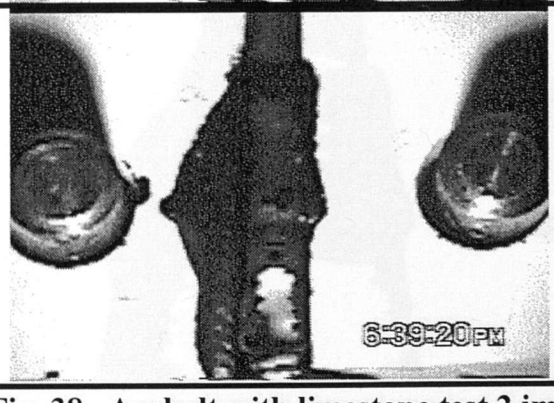

Fibril	8	
Real Time	6:39:20	
Elapse Time	0:00:13	
Coordinates	X	Y
Fibril Left End	140	232
Fibril Right End	163	232
Fibril Top	149	231
Fibril Bottom	150	234

Fig. 38 Asphalt with limestone test 2 images 5-8.

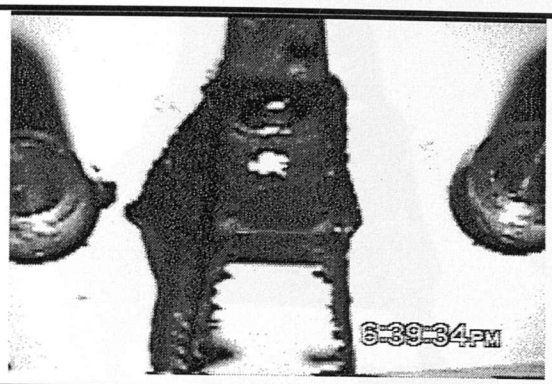

Fibril	9	
Real Time	6:39:34	
Elapse Time	0:00:27	
Coordinates	X	Y
Fibril Left End	126	143
Fibril Right End	178	144
Fibril Top	153	143
Fibril Bottom	154	147

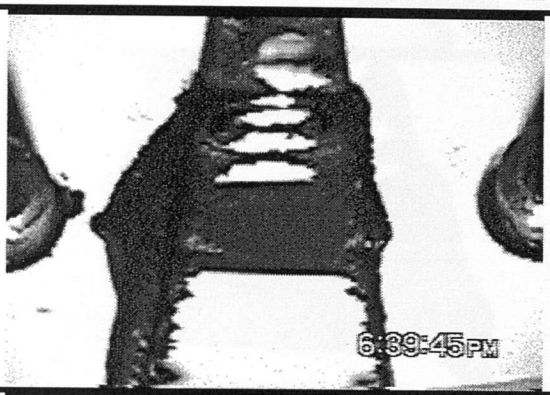

Fibril	10	
Real Time	6:39:45	
Elapse Time	0:00:38	
Coordinates	X	Y
Fibril Left End	140	61
Fibril Right End	174	61
Fibril Top	159	60
Fibril Bottom	158	62

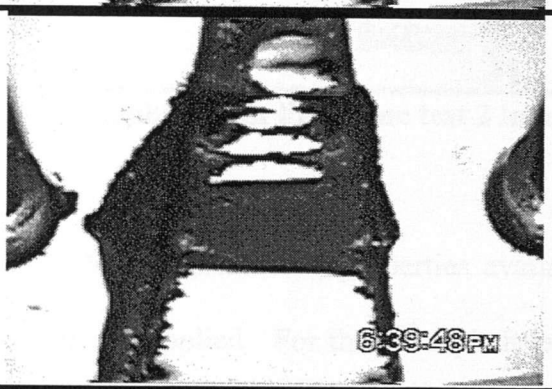

Fibril	11	
Real Time	6:39:48	
Elapse Time	0:00:41	
Coordinates	X	Y
Fibril Left End	137	52
Fibril Right End	193	52
Fibril Top	158	51
Fibril Bottom	158	54

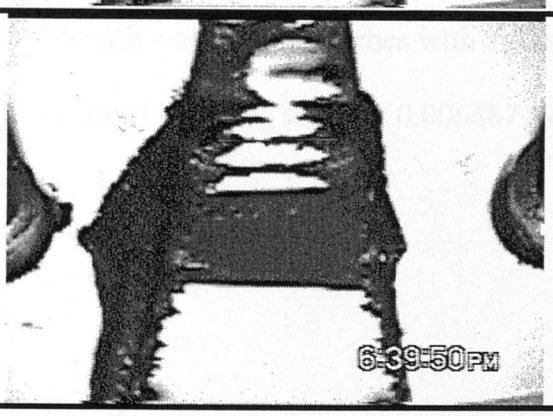

Fibril	12	
Real Time	6:39:50	
Elapse Time	0:00:43	
Coordinates	X	Y
Fibril Left End	122	77
Fibril Right End	189	76
Fibril Top	144	76
Fibril Bottom	145	79

Fig. 39 Asphalt with limestone test 2 images 9-12.

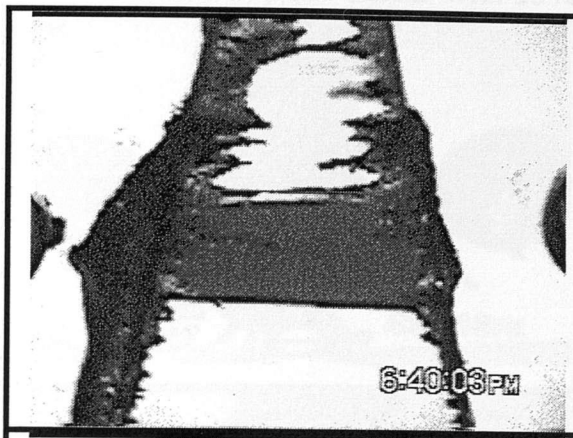

Fibril	13	
Real Time	6:40:03	
Elapse Time	0:00:56	
Coordinates	X	Y
Fibril Left End	102	102
Fibril Right End	208	102
Fibril Top	134	101
Fibril Bottom	134	103

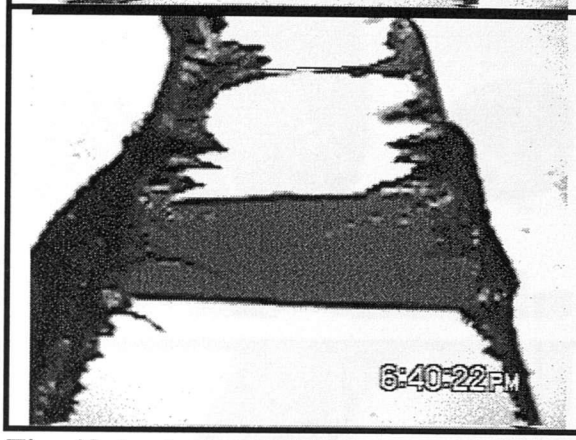

Fibril	14	
Real Time	6:40:22	
Elapse Time	0:01:15	
Coordinates	X	Y
Fibril Left End	112	34
Fibril Right End	218	30
Fibril Top	159	33
Fibril Bottom	159	34

Fig. 40 Asphalt with limestone test 2 images 13 & 14.

With the material properties available, the analysis explained in the previous section was applied. For the 2nd asphalt test it was determined that the average critical fibril length was 0.09518 inches with a standard deviation of 0.0893. While the average critical fibril breaking width is 0.006687 inches with a standard deviation of 0.0024396.

AAM-1 Asphalt binder with 25% limestone, Test 3

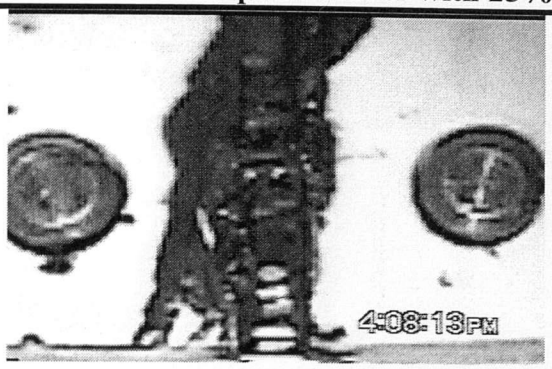

Fibril	1	
Real Time	4:08:13	
Elapse Time	0:00:07	
Coordinates	X	Y
Fibril Left End	290	397
Fibril Right End	328	386
Fibril Top	315	388
Fibril Bottom	317	393

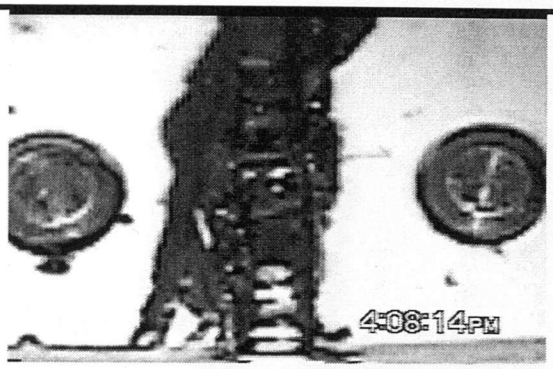

Fibril	2	
Real Time	4:08:14	
Elapse Time	0:00:08	
Coordinates	X	Y
Fibril Left End	276	447
Fibril Right End	342	446
Fibril Top	315	444
Fibril Bottom	316	449

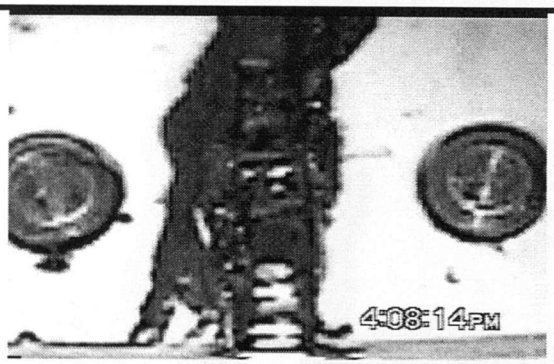

Fibril		
Real Time	3	
Elapse Time	4:08:14	
Coordinates	0:00:08	
Fibril Left End	X	Y
Fibril Right End	282	371
Fibril Top	326	369
Fibril Bottom	310	364
	311	375

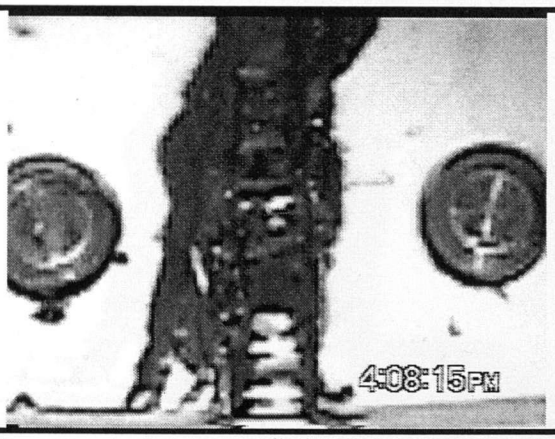

Fibril	4	
Real Time	4:08:15	
Elapse Time	0:00:09	
Coordinates	X	Y
Fibril Left End	294	234
Fibril Right End	325	231
Fibril Top	306	226
Fibril Bottom	306	241

Fig. 41 Asphalt with limestone test 3 images 1-4.

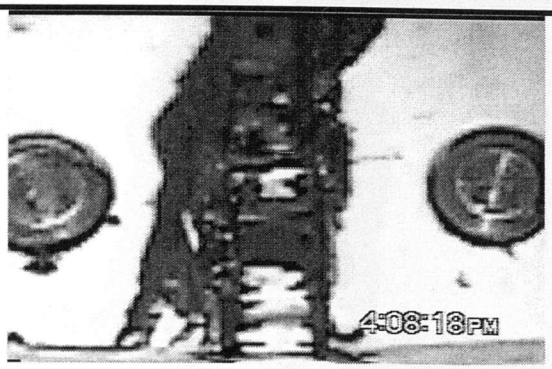

Fibril	5	
Real Time	4:08:18	
Elapse Time	0:00:12	
Coordinates	X	Y
Fibril Left End	294	190
Fibril Right End	328	191
Fibril Top	311	187
Fibril Bottom	310	196

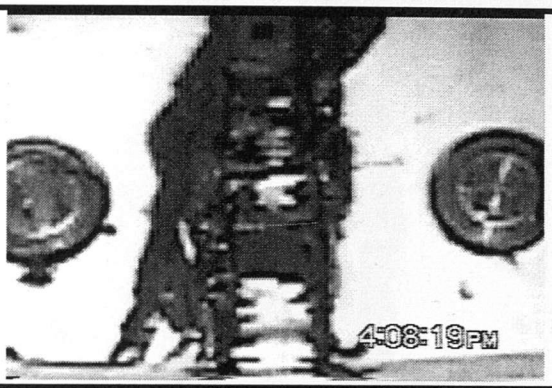

Fibril	6	
Real Time	4:08:19	
Elapse Time	0:00:13	
Coordinates	X	Y
Fibril Left End	260	281
Fibril Right End	357	275
Fibril Top	308	262
Fibril Bottom	311	288

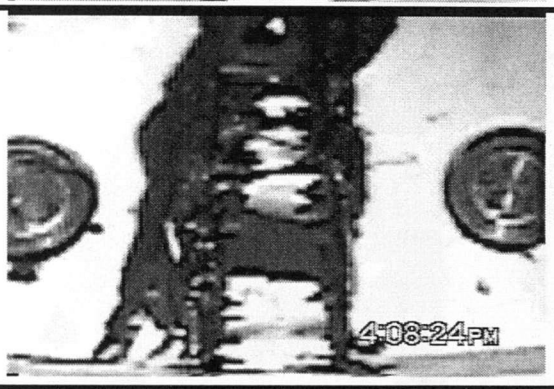

Fibril	7	
Real Time	4:08:24	
Elapse Time	0:00:18	
Coordinates	X	Y
Fibril Left End	275	157
Fibril Right End	350	184
Fibril Top	307	165
Fibril Bottom	301	174

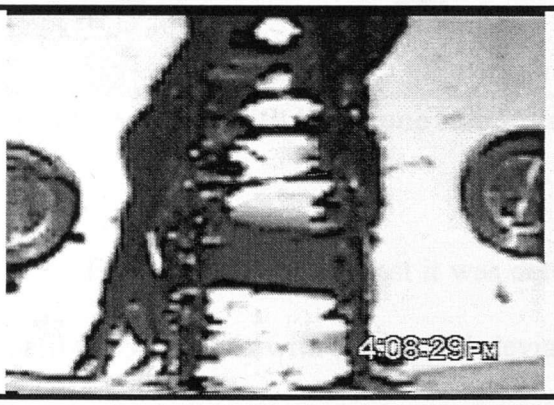

Fibril	8	
Real Time	4:08:29	
Elapse Time	0:00:23	
Coordinates	X	Y
Fibril Left End	250	216
Fibril Right End	369	203
Fibril Top	311	208
Fibril Bottom	311	213

Fig. 42 Asphalt with limestone test 3 images 5-8.

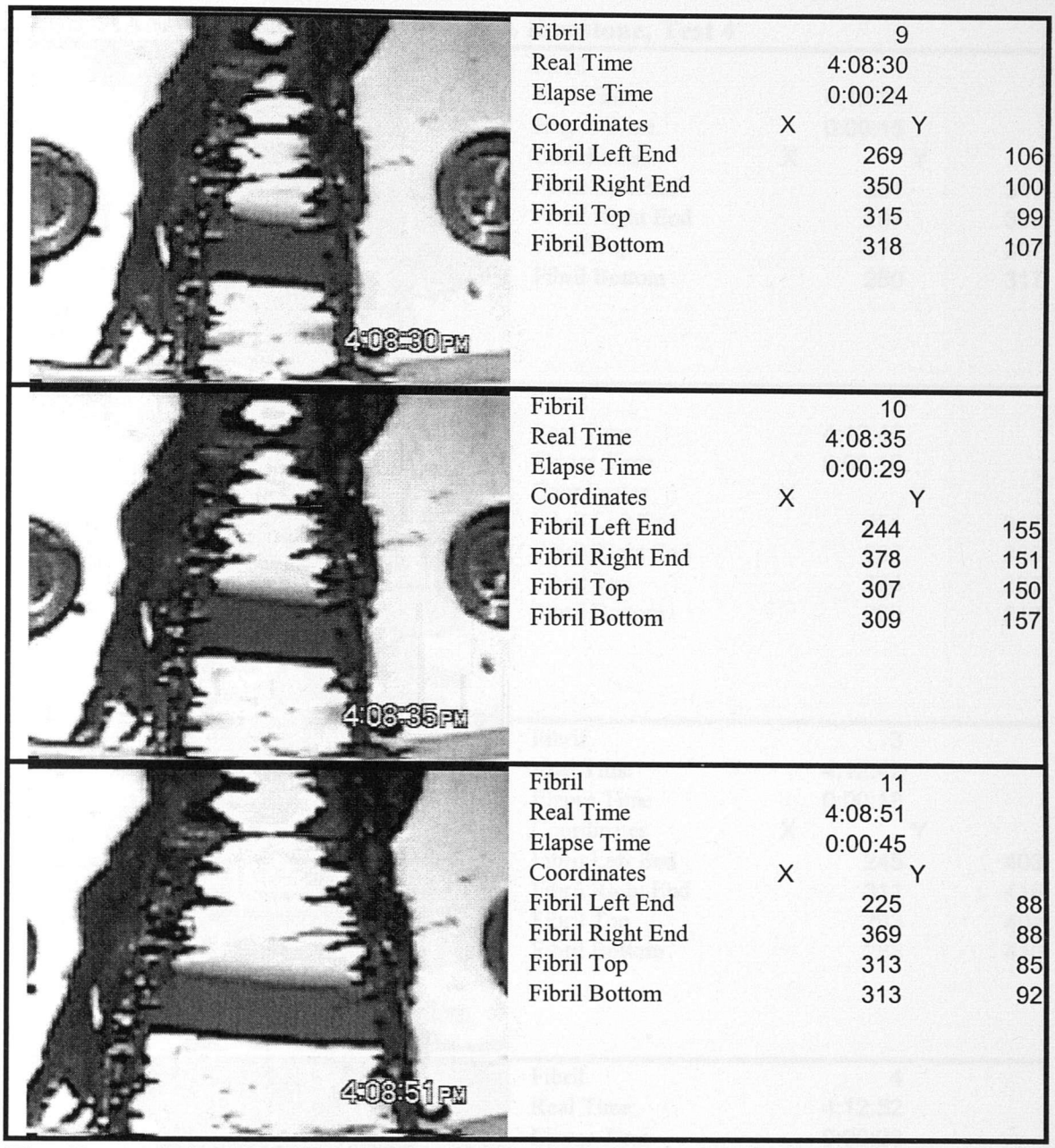

Fig. 43 Asphalt with limestone test 3 images 9-11.

For the third asphalt test it was determined that the average critical fibril length was 0.08098 inches with a standard deviation of 0.06378. While the average critical fibril breaking width is 0.01027 inches with a standard deviation of 0.008959.

AAM-1 Asphalt binder with 25% limestone, Test 4

Fibril	1	
Real Time	4:12:39	
Elapse Time	0:00:15	
Coordinates	X	Y
Fibril Left End	251	317
Fibril Right End	297	308
Fibril Top	274	307
Fibril Bottom	280	317

Fibril	2	
Real Time	4:12:40	
Elapse Time	0:00:16	
Coordinates	X	Y
Fibril Left End	251	317
Fibril Right End	297	308
Fibril Top	274	307
Fibril Bottom	280	317

Fibril	3	
Real Time	4:12:42	
Elapse Time	0:00:18	
Coordinates	X	Y
Fibril Left End	245	403
Fibril Right End	311	416
Fibril Top	283	404
Fibril Bottom	283	416

Fibril	4	
Real Time	4:12:52	
Elapse Time	0:00:28	
Coordinates	X	Y
Fibril Left End	218	374
Fibril Right End	312	402
Fibril Top	286	384
Fibril Bottom	283	399

Fig. 44 Asphalt with limestone test 4 images 1-4.

Fibril		5
Real Time		4:12:52
Elapse Time		0:00:28
Coordinates	X	Y
Fibril Left End	198	445
Fibril Right End	364	471
Fibril Top	260	454
Fibril Bottom	256	458

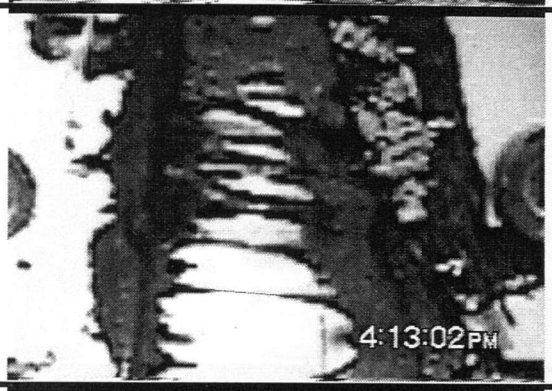

Fibril		6
Real Time		4:13:02
Elapse Time		0:00:38
Coordinates	X	Y
Fibril Left End	174	357
Fibril Right End	385	375
Fibril Top	269	365
Fibril Bottom	269	366

Fibril		7
Real Time		4:13:23
Elapse Time		0:00:59
Coordinates	X	Y
Fibril Left End	149	198
Fibril Right End	402	240
Fibril Top	284	221
Fibril Bottom	281	231

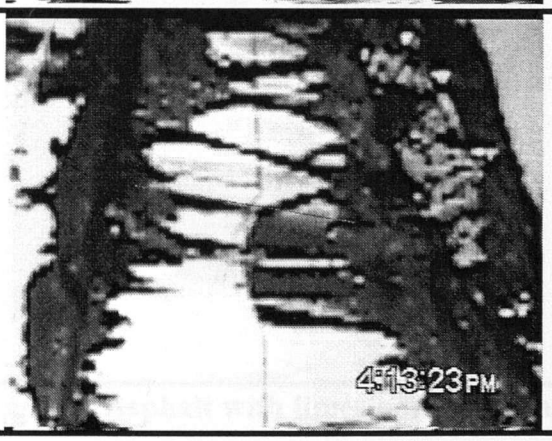

Fibril		8
Real Time		4:13:24
Elapse Time		0:01:00
Coordinates	X	Y
Fibril Left End	115	313
Fibril Right End	443	354
Fibril Top	264	332
Fibril Bottom	264	333

Fig. 45 Asphalt with limestone test 4 images 5-8.

Fibril	9	
Real Time	4:13:31	
Elapse Time	0:01:07	
Coordinates	X	Y
Fibril Left End	220	79
Fibril Right End	367	71
Fibril Top	292	73
Fibril Bottom	295	83

Fibril	10	
Real Time	4:13:32	
Elapse Time	0:01:08	
Coordinates	X	Y
Fibril Left End	144	143
Fibril Right End	386	200
Fibril Top	265	166
Fibril Bottom	264	171

Fibril	11	
Real Time	4:13:35	
Elapse Time	0:01:11	
Coordinates	X	Y
Fibril Left End	219	108
Fibril Right End	394	135
Fibril Top	278	116
Fibril Bottom	278	124

Fibril	12	
Real Time	4:13:54	
Elapse Time	0:01:30	
Coordinates	X	Y
Fibril Left End	82	297
Fibril Right End	559	347
Fibril Top	341	323
Fibril Bottom	341	329

Fig. 46 Asphalt with limestone test 4 images 9-12.

Fig. 47 Asphalt with limestone test 4 image 13.

For the fourth asphalt test it was determined that the average critical fibril length was 0.2397 inches with a standard deviation of 0.1718. While the average critical fibril breaking width is 0.009232 inches with a standard deviation of 0.006513.

AAM-1 Asphalt binder with 25% limestone, Test 5

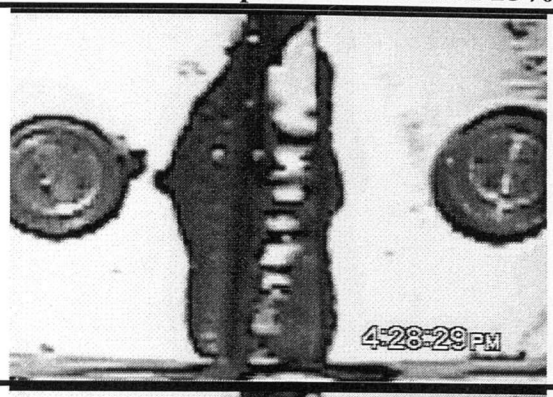

Fibril	1	
Real Time	4:28:29	
Elapse Time	0:00:08	
Coordinates	X	Y
Fibril Left End	289	361
Fibril Right End	324	360
Fibril Top	299	356
Fibril Bottom	303	363

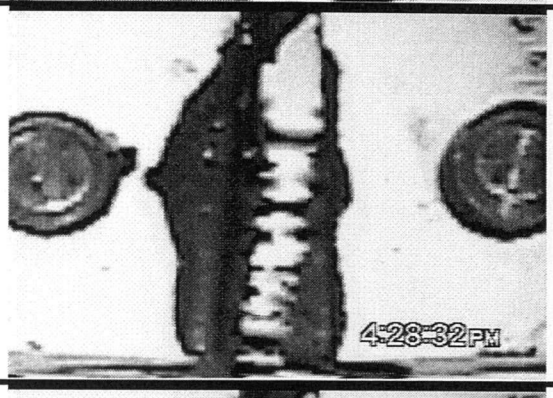

Fibril	2	
Real Time	4:28:31	
Elapse Time	0:00:10	
Coordinates	X	Y
Fibril Left End	285	286
Fibril Right End	342	287
Fibril Top	311	285
Fibril Bottom	310	291

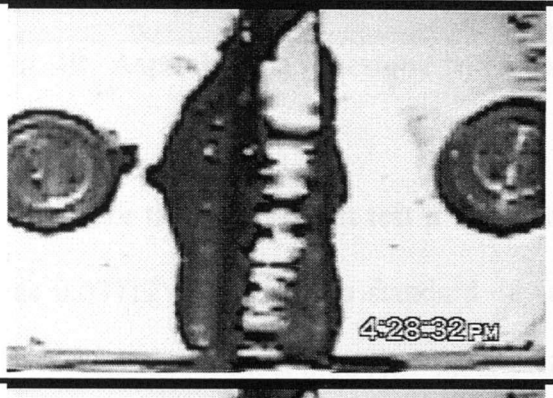

Fibril	3	
Real Time	4:28:32	
Elapse Time	0:00:11	
Coordinates	X	Y
Fibril Left End	278	335
Fibril Right End	337	340
Fibril Top	301	334
Fibril Bottom	299	343

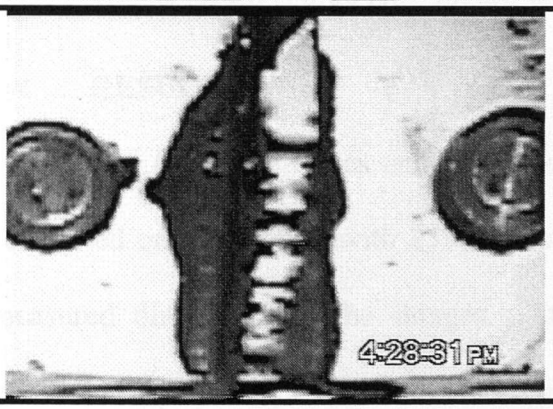

Fibril	4	
Real Time	4:28:32	
Elapse Time	0:00:11	
Coordinates	X	Y
Fibril Left End	264	396
Fibril Right End	330	403
Fibril Top	292	398
Fibril Bottom	293	406

Fig. 48 Asphalt with limestone test 5 images 1-4.

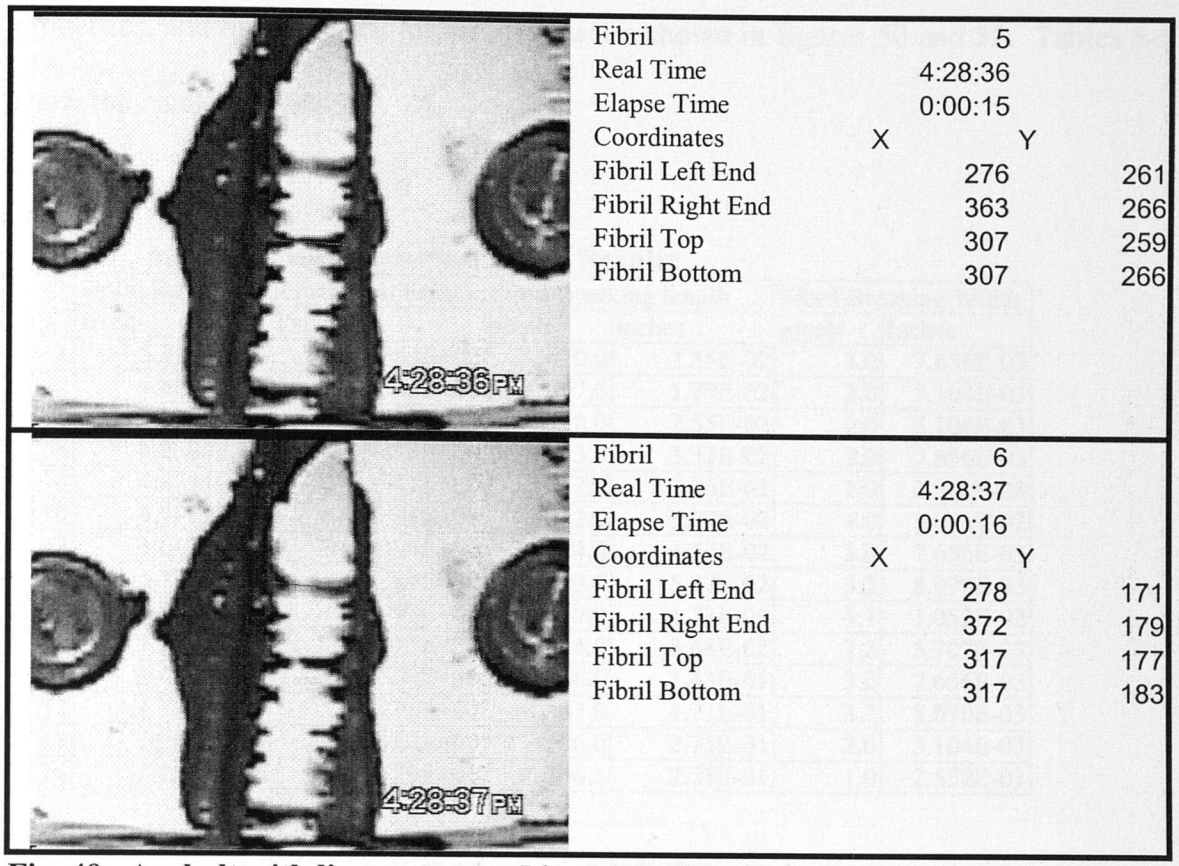

Fig. 49 Asphalt with limestone test 5 images 5 & 6.

For the fifth asphalt test it was determined that the average critical fibril length was 0.03712 inches with a standard deviation of 0.04778. While the average critical fibril breaking width is 0.004132 inches with a standard deviation of 0.005056.

4.4 RESULTS

The following tables and figures are a summary of the results of the four test conducted on the asphalt with 25% limestone. Fibril breaking length and width were measured directly from the images. Strain rate was calculated by virtue of that individual fibril location. Failure traction is a function of the strain rate, material

properties, and time of fibril failure. These are shown in figures 50 and 51. Tables 5-8 show the results of tests 2-5.

Table 5 Asphalt with Limestone Test 2 Results

	Strain Rates	Traction at Failure	Fibril Breaking length		Fibril Breaking Width	
	1/sec.	Psi	pixels	inches	pixels	Inches
1	5.2177E-03	5.9363E+00	10.0	2.55E-02	3.0	7.656E-03
2	4.8637E-03	5.5335E+00	7.0	1.79E-02	2.0	5.104E-03
3	5.0461E-03	5.7410E+00	10.0	2.55E-02	2.0	5.104E-03
4	5.2284E-03	5.9485E+00	13.0	3.32E-02	3.0	7.656E-03
5	4.8744E-03	6.1617E+00	12.0	3.06E-02	1.0	2.552E-03
6	4.5419E-03	7.4631E+00	12.0	3.07E-02	4.0	1.021E-02
7	4.6491E-03	7.6394E+00	14.0	3.57E-02	3.0	7.656E-03
8	5.3786E-03	8.8380E+00	23.0	5.87E-02	3.2	8.070E-03
9	4.4239E-03	1.5093E+01	52.0	1.33E-01	4.1	1.052E-02
10	3.5442E-03	1.7015E+01	34.0	8.68E-02	2.2	5.707E-03
11	3.4477E-03	1.7858E+01	56.0	1.43E-01	3.0	7.656E-03
12	3.7158E-03	4.2276E+00	67.0	1.71E-01	3.2	8.070E-03
13	3.9840E-03	2.8182E+01	106.0	2.71E-01	2.0	5.104E-03
14	3.2546E-03	3.0829E+01	106.1	2.71E-01	1.0	2.552E-03

	Inches	STD
Average Fibril Length	9.518E-02	0.0893477
Average Fibril Width	6.687E-03	0.0024396

Table 6 Asphalt with Limestone Test 3 Results

	Strain Rates	Traction at Failure	Fibril Breaking length		Fibril Breaking Width	
	1/sec.	Psi	pixels	inches	pixels	Inches
1	5.0101E-03	4.4338E+00	39.6	5.15E-02	5.4	7.012E-03
2	5.2838E-03	5.3437E+00	66.0	8.59E-02	5.1	6.639E-03
3	4.8678E-03	4.9231E+00	44.0	5.74E-02	11.0	1.438E-02
4	4.1180E-03	4.6852E+00	31.1	4.06E-02	15.0	1.953E-02
5	3.8772E-03	5.8810E+00	34.0	4.43E-02	9.1	1.179E-02
6	4.3753E-03	7.1893E+00	97.2	1.27E-01	26.2	3.408E-02
7	3.6966E-03	8.4093E+00	79.7	1.04E-01	10.8	1.408E-02
8	4.0195E-03	1.1683E+01	119.7	1.56E-01	5.0	6.510E-03
9	3.4175E-03	1.0365E+01	81.2	1.06E-01	8.5	1.113E-02
10	3.6856E-03	1.3505E+01	134.1	1.75E-01	7.3	9.479E-03
11	3.3189E-03	1.8868E+01	144.0	1.87E-01	7.0	9.115E-03

	Inches	STD
Average Fibril Length	8.098E-02	6.387E-02
Average Fibril Width	1.027E-02	8.959E-03

Table 7 Asphalt with Limestone Test 4 Results

	Strain Rates	Traction at Failure	Fibril Breaking length		Fibril Breaking Width	
	1/sec.	Psi	pixels	inches	pixels	inches
1	4.5723E-03	8.6685E+00	46.9	6.10E-02	11.7	1.518E-02
2	4.5723E-03	9.2462E+00	46.9	6.10E-02	11.7	1.518E-02
3	5.0430E-03	1.1472E+01	67.3	8.76E-02	12.0	1.562E-02
4	4.8843E-03	1.7281E+01	98.1	1.28E-01	15.3	1.992E-02
5	5.2729E-03	1.8656E+01	168.0	2.19E-01	5.7	7.366E-03
6	4.7912E-03	2.3002E+01	211.8	2.76E-01	1.0	1.302E-03
7	3.9210E-03	2.9221E+01	256.5	3.34E-01	10.4	1.359E-02
8	4.5504E-03	3.4486E+01	330.6	4.30E-01	1.0	1.302E-03
9	3.2697E-03	2.7670E+01	147.2	1.92E-01	10.4	1.359E-02
10	3.6200E-03	3.1091E+01	248.6	3.24E-01	5.1	6.639E-03
11	3.4284E-03	3.3341E+01	177.1	2.31E-01	8.0	1.042E-02
12	4.4628E-03	5.0725E+01	479.6	6.24E-01	6.0	7.812E-03
13	3.5433E-03	4.0721E+01	298.9	3.89E-01	1.0	1.302E-03

	Inches	STD
Average Fibril Length	2.397E-01	1.718E-01
Average Fibril Width	9.232E-03	6.513E-03

Table 8 Asphalt with Limestone Test 5 Results

	Strain Rates	Traction at Failure	Fibril Breaking length		Fibril Breaking Width	
	1/sec.	Psi	Pixels	inches	pixels	inches
1	4.8131E-03	4.8677E+00	35.0	4.56E-02	8.1	1.050E-02
2	4.4026E-03	5.5653E+00	57.0	7.42E-02	6.1	7.920E-03
3	4.6708E-03	6.4946E+00	59.2	7.71E-02	9.2	1.200E-02
4	5.0047E-03	6.9588E+00	66.4	8.64E-02	8.1	1.050E-02
5	4.2658E-03	8.0874E+00	87.1	1.13E-01	7.0	9.115E-03
6	3.7732E-03	7.6303E+00	94.3	1.23E-01	6.0	7.812E-03

	Inches	STD
Average Fibril Length	3.712E-02	4.778E-02
Average Fibril Width	4.132E-03	5.056E-03

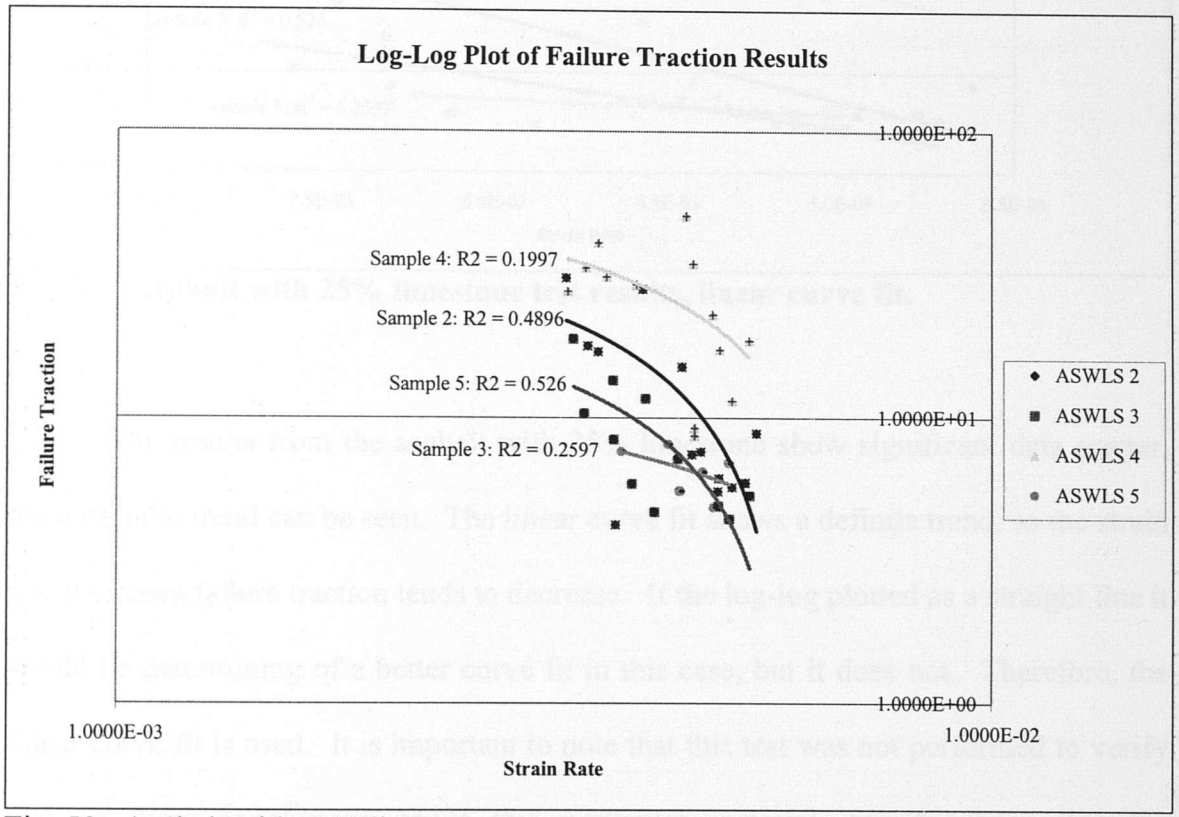

Fig. 50 Asphalt with 25% limestone test results, log-log plot.

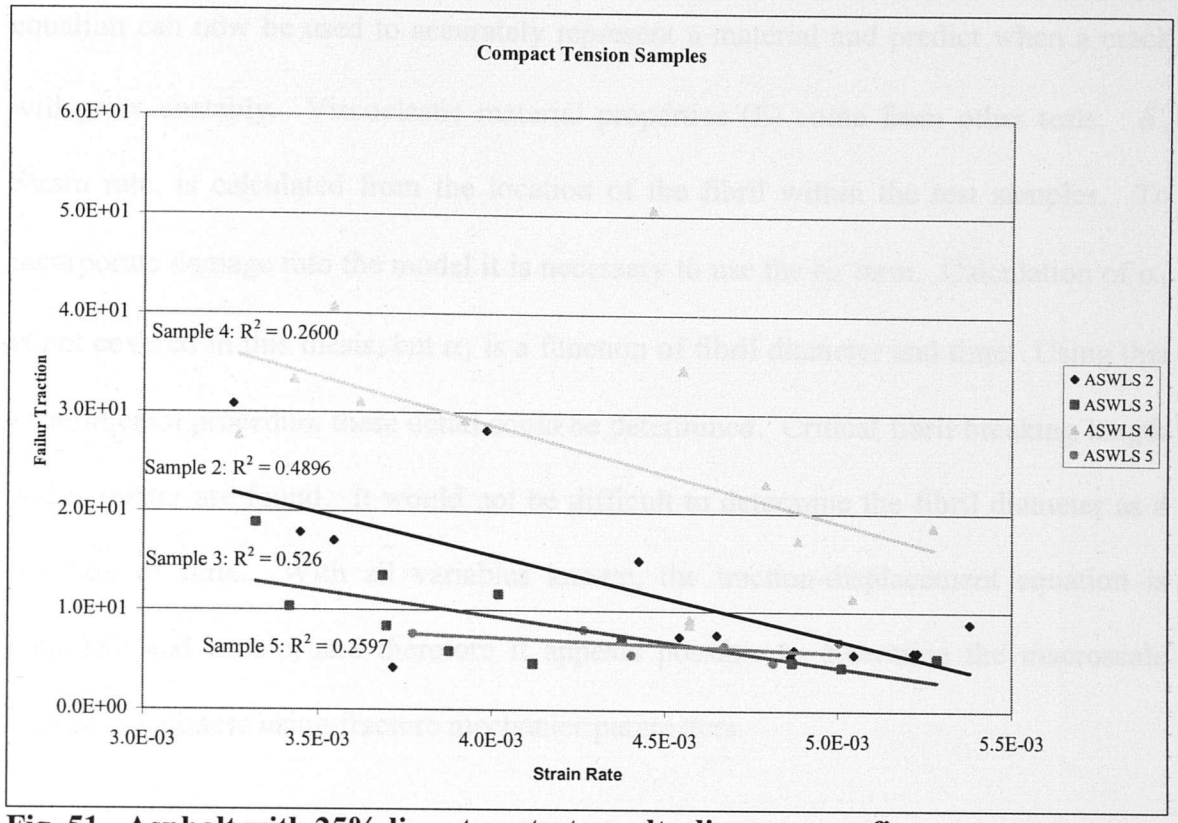

Fig. 51 Asphalt with 25% limestone test results, linear curve fit.

The results from the asphalt with 25% limestone show significant data scatter, but a definite trend can be seen. The linear curve fit shows a definite trend, as the strain rate increases failure traction tends to decrease. If the log-log plotted as a straight line it would be determining of a better curve fit in this case, but it does not. Therefore, the linear curve fit is used. It is important to note that this test was not performed to verify that or draw conclusions about this particular material, but to show that the experimental procedure is valid for an extensive study to do so.

In essence, the experiment detailed here reveals how all unknowns in the traction-displacement equation (1) can now be found. With all variables known the

equation can now be used to accurately represent a material and predict when a crack will grow unstably. Viscoelastic material properties (E) come from other tests. $\dot{\delta}$, Strain rate, is calculated from the location of the fibril within the test samples. To incorporate damage into the model it is necessary to use the α_1 term. Calculation of α_1 is not covered in this thesis, but α_1 is a function of fibril diameter and time. Using this experimental procedure these detail could be determined. Critical fibril breaking length and diameter are found. It would not be difficult to determine the fibril diameter as a function of time. With all variables known, the traction-displacement equation is complete and usable, and therefore it appears possible to determine the macroscale fracture toughness using fracture mechanics parameters.

CHAPTER V

CONCLUSIONS AND RECOMMENDATIONS

In conclusion, these experiments have proven to be a useful way to gather geometric measurements of specific cohesive zone parameters in viscoelastic materials. From the video collected the crack tip opening, damage zone profile ahead of the crack tip, crack tip opening rate, critical fibril breaking length and diameter can all be measured. This information is critical in characterizing and using the viscoelastic cohesive zone model. However, it is not valid for all materials. It has proven to be very difficult, even with this procedure, to produce quality video of fibrils and cohesive zones. As previously mentioned, fibrils in certain materials are extremely small, and may not be seen with this procedure. Highly ductile, viscoelastic materials tested at quasi-static velocities seem to produce the best results. One of the next steps in this experiment is to develop an effective method for fatigue testing of materials. Fatigue testing of samples seems to develop more pronounced or definitive cohesive zones. The more pronounced the cohesive zone is the easier it will be to produce a video of a cohesive zone ahead of a propagating crack tip.

The results of this thesis have been very successful. Two experiments for measuring specific cohesive zone parameters have been developed. The first experiment outlined is useful for testing materials with large cohesive zones, between one half millimeter and two inches. The smallest cohesive zone viewable with the stereomicroscope is on the order of 0.25 mm. However, depth of field is significantly limited at that magnification, and therefore may not be practical. With high definition

cameras, higher quality optics and image enhancement software, smaller cohesive zones may potentially be viewed optically. This equipment is also capable of testing materials with cohesive zones as large as two inches. This procedure does not require the use of the stereomicroscope, the optics and zoom of this Handicam is sufficient. For more in-depth studies a higher quality camera is recommended for this; one with a large optical zoom. This would reduce image distortion at extreme telephoto zoom. This procedure was used for testing the asphalt with 25% limestone and image degradation at extreme digital magnification was evident.

The most limiting factors in this experiment are the motors applying the load and the quality of the cameras and/or optics. The standard Nanomotion II motors are limited to pushing 20 kg. according to the product specifications. In reality, it was difficult to produce half that amount of force. Melles Griot produces high torque motors that are designed to push as much as 40kgs. These may be a worthy investment for testing tougher materials. Much stronger stepper motors are commercially available from other companies and could bė configured to do this experiment. Generally the stronger motors don't have as fine a movement, but depending on the materials this may not be a problem.

Analytically, the cameras and optics are the most limiting factor. The Zeiss SV8 stereomicroscope is sufficient for magnification and image quality. The Panasonic cameras that were inserted into the eyepieces for collecting the images are where most of the image degradation occurred. The camera's pick-up devise is only ½ inch in width and only captured about half what is normally viewed through the eyepiece. For long

term testing with the stereomicroscope, it is recommended that a larger camera with a higher resolution picture be used. This would dramatically increase the quality and accuracy of the analysis that could be performed.

A digital video camera is highly recommended for recording the images, especially if the tests are done without the stereomicroscope and solely with the camera optics. A professional quality digital video camera like the Canon GL1 (approx. $2200 retail) or XL1 (approx. $4200 retail) would produce better results for several reasons. One, the digital format allows for much easier transfer of data to the computer through firewire technology. This would remove the need for the Belkin Videobus II hardware. Images would be initially recorded digitally with superior pixel resolution. Two, the quality of the optics for tests not using the stereomicroscope would be dramatically increased. The XL1 camera has the ability to use a variety of different XL optics as well use any Canon EOS EF lens. Therefore, an optical lens specifically designed for that magnification and focal point could be selected. With macro lenses and 3D stereoscopic lenses available, the optical flexibility of this system is unmatched. Both the XL1 and the GL1 cameras have the ability to record up to 80 mins. of video as high-resolution stills. This is exactly the kind of format that will optimize results.

As mentioned at the beginning of the chapter, digital video is very memory intensive. For any kind of study into a specific material, with current levels of technology, a computer with at least 40 gigabytes (GB) of hard drive space, 256 megabytes (MB) of RAM, and a CD burner are an absolute necessity. In fact, the largest hard drive and the most RAM that can be afforded is recommended. The CD burner will

prove invaluable in long term storage of tests. If it can be afforded, a DVD burner is worthy of consideration. Digital Video Disks (DVD) are designed for holding the large files associated with large quantities of digital video without reducing image quality. Currently writable CD ROM's hold 800 MB whereas writable DVD ROM's can hold as much as 5 GB or more.

For an extensive study into any material better image analysis software is required. The software used for this development proved effective and functional, but not particularly suited for scientific analysis. Although it was not used or tested, Image Pro Plus was reviewed. This kind of software is specifically designed for image capturing and scientific analysis. Image Pro Plus can serve all functions needed for this experiment. It can capture, measure, analyze, and catalog or archive all the data. The only reason not to use this software, or one like it, is the cost. At $4500 a copy, it may not be cost effective.

The second experiment is used for much smaller cohesive zones. This should be used for testing any materials that have cohesive zones smaller than what can be viewed using optics. Some materials will require an operator's judgement call on whether to use the optical or ESEM testing procedure. Optical testing is usually preferred because long term SEM tests can incur extensive operating costs. However, it should be noted that the reduced depth of field found at high optical magnification is significantly reduced inside the SEM. Conversely, there have been major advances in software technology that can remove this problem. Multiple images at varying focal points can be digitally combined to produce one image with enhanced depth of field.

For certain materials it will not be possible to make cohesive zone images optically. For these materials the SEM is an absolute necessity. The tensile stage developed for use in Texas A&M's ESEM is exactly the kind of equipment that is required for this kind of research. The next step in the development of this piece of equipment would be to increase its versatility. Currently the stage will only work on an Electroscan ESEM, and has limited control over the movement of the grips. The first step towards increasing control is to add an independent drive system. The current system uses the ESEM's stepper motors and is not sensitive to start/stop controls or the rate at which they open and close. An independent stepper motor, one able to perform its duties in the vacuum chamber and be computer controlled, is a logical choice.

A more versatile baseplate should also be developed. If a motor were attached to the system, a new baseplate would be designed anyway. It only seems logical to design the plate to fit several different microscopes. Potentially, the baseplate could be designed to fit the ESEM, a SEM and an atomic force microscope (AFM). This kind of versatility would allow for vast improvements in data collection. The material could then be coupled with the scope most suited to produce the best images. In addition, materials could be tested and video taped in multiple microscopes. This produces more kinds of data and therefore can help to confirm conclusions.

If a motor and a new base plate are added to the system, it would remove the need for the Nanomotion II optical stage. The new tensile stage could potentially do the job of both stages. It is also recommeneded that the pins continue to be developed. They function, but need to work better. They need to hold the samples so that they only

fail at the crack tip. Currently there is too much crack tip movement to acquire usable date for electron microscope analysis.

In conclusion, the development of two experiments for measuring specific cohesive zone parameters is successful, but requires further development and investigation. This initial development presents a methodology for producing cohesive zone images and measurements of parameters within. Further development is required and recommended to increase the optical image quality as well as displacement control for both optical and ESEM experiments. Better cameras will increase the optical picture quality. New software will easily increase measurement accuracy for either procedure. For optical experiments, different motors could increase potential load application, but may reduce movement sensitivity. This may or may not be a problem, depending on the material to be tested. ESEM experimental development should involve the addition of an independent drive system as well as baseplate modification. At a minimum, the baseplate will need modification to incorporate the addition of a motor to the system. It is recommended that the at that point the baseplate be made for use with several different microscopes to increase versatility.

With or without the changes, the experiments herein will produce accurate numbers for all parameters used in the Allen-Searcy traction-displacement cohesive zone model (equation 1). With accurate numbers unstable crack development in viscoelastic materials can be predicted better than ever before.

REFERENCES

Allen, D.H., and C.R. Searcy, 2001a "A Micromechanically-Based Model for Predicting Dynamic Damage Evolution in Ductile Polymers," accepted by *Mechanics of Materials*.

Allen, D.H., and C.R. Searcy, 2001b "A Micromechanical Model for a Viscoelastic Cohesive Zone," *International Journal of Fracture*, Vol. 107, p. 159.

Beahan, P., Beavis, M., and D. Hull, 1971 "The Morphology of Crazes in Polystyrene," *The Philosophical Magazine*, Vol. 24, No. 192, p. 1267.

Corleto, C.R., Bradley, W.L., and H.F. Brinson, 1996, "An Experimental Micromechanics Measurement Technique for Submicrometre Domains," *Journal of Material Science*, Vol. 31, p. 1803.

Hertzberg, R.W., 1987 "Fracture Surface Micromorphology in Engineering Solids," *Fractography of Modern Engineering Materials: Composites and Metals*, ASTM STP 948, p. 5.

Hibbs, M.F. and W.L. Bradley, 1987 "Correlations Between Micromechanical Failure Processes an the Delamination Toughness of Graphite/Epoxy Systems," *Fractography of Modern Engineering Materials: Composites and Metals*, ASTM STP 948, p. 17, p. 68.

Hull, D., 1999, *Fractography Observing, Measuring and Interpreting Fracture Surface Topography*, Cambridge University Press, Cambridge, p. 219.

Pandya, K.C., and J.G. Williams, 2000a, "Measurement of Cohesive Zone Parameters in Tough Polyethylene," *Polymer Engineering and Science*, Vol. 40, p. 1765.

Pandya, K.C., and J.G. Williams, 2000b, "Cohesive zone Modelling of Crack Growth in Polymers Part 1-Experimental Measurement of Cohesive Law," *Plastics Rubber and Composites*, Vol. 29, p. 439.

Pandya, K.C., and J.G. Williams, 2000c, "Cohesive Zone Modelling of Crack Growth in Polymers Part 2-Numerical Simulation of Crack Growth," *Plastics Rubber and Composites*, Vol. 29, p. 447

Sue, H.J., 1991, "Study of Robber-Modified Brittle Epoxy Systems. Part 1: Fracture Toughness Measurements Using the Double-Notch Four-Point-Bend Method," *Polymer Engineering and Science*, Vol. 31, p. 270.

Suresh, S., 1991 *Fatigue of Materials*, Cambridge University Press, Cambridge, p. 456.

Wang, W.V., and Kramer, E. J., 1982a, "A Distributed Dislocation Stress Analysis for Crazes and Plastic Zones at Crack tips," *Journal of Material Science*, Vol. 17, p. 2013.

Wang, W.V., and E. J. Kramer, 1982b, "The Micromechanics and Microstructure of CO2 Crazes in Polystyrene," *Polymer*, Vol. 23, p. 1667.

Washiyama, J., Creton, C., and E.J. Kramer, 1992, "TEM Fracture Studies of Polymer Interfaces," *Macromolecules*, Vol. 25, p.4751.

Yang, A.C.M., Kramer, E. J., Kuo, C.C., and S.L. Phoenix, 1986, "Craze Fibril Stability and Breakdown in Polystyrene," *Macromolecules*, Vol. 19, p. 2010.

APPENDIX

The CD-ROM attached to this thesis contains four digital video files. Each file is the original video used for the development of the analysis procedure compressed with winzip. The files are labeled as Asphalt with Limestone 2, 3, 4, and 5. Each video is in **.avi video format. A computer with a CD-ROM as well as software capable of reading **.avi files is required to view each of the tests. Before the video can be viewed each fill will need to be unzipped, or decompressed. The winzip.exe file on the cd will install the winzip program that will decompress each file to the computers hard drive or specified location. After the files have been decompressed the can be viewed with a **.avi viewing program.

VITA

Justin Joel Williams was born on October 8, 1976 in Borger, Texas. He moved to New York at a young age and grew up in the upstate area. He graduated from Groton Jr. & Sr. High School. In December 1999 he earned a Bachelor of Science degree from Embry-Riddle Aeronautical University in Aerospace Engineering and moved directly into a Master of Science program at Texas A&M University in the same subject. His mother's address, where he can be reached, is 4198 Pine View Drive, Gillsville, GA 30543.